TFAM-dependent mitochondrial integrity in regulatory T cells preserves immune landscape and restrains inflammaging

Kai Guo[1, 2, $], Zhihan Wang[3, 4, $], Jappreet Singh Gill[3, $], Trishna Debnath[3], Benu Bansal[2, 3, 9], Rayansh Poojary[3], Jacquiline Kim Correa[3], Hakan Celik[3], Het Mehta[3], Eden Abrham[3], Zachery Even[3], Mansib Rahman[3], Abby Lund Da Costa[3], Shilpi Jain[3], Xusheng Wang[5], Gopal Murugaiyan[6], Adrian T. Ting[7], Junguk Hur[2], Nadeem Khan[8], Holly Brown-Borg[2], Donald A Jurivich[3], Ramkumar Mathur[3, *]

1. Department of Neurology, University of Michigan, Ann Arbor, MI 48109, USA
2. Department of Biomedical Sciences, School of Medicine and Health Sciences, University of North Dakota, Grand Forks, ND 58202, USA
3. Department of Geriatrics, School of Medicine and Health Sciences, University of North Dakota, Grand Forks, ND 58202, USA
4. West China School of Basic Medical Sciences & Forensic Medicine, Sichuan University, Chengdu, Sichuan, China
5. Department of Neurology, University of Tennessee Health Science Center, Memphis, TN 38163, USA
6. Ann Romney Center for Neurologic Diseases, Brigham and Women's Hospital, Boston and Harvard Medical School, Boston, MA 02115, USA
7. Department of Immunology, Mayo Clinic, Rochester, MN 55905, USA
8. Dept of Oral Biology, College of Dentistry, University of Florida, Gainesville, FL 32603, USA
9. Department of Biomedical Data Science, School of Applied Computational Sciences, Meharry Medical College, Nashville, TN 37208, USA

[$]Authors (Kai Guo, Zhihan Wang and Jappreet Singh Gill) contributed equally

*Correspondence
Ramkumar Mathur, Department of Geriatrics, School of Medicine and Health Sciences, University of North Dakota, Grand Forks, ND 58202, USA
Email: ramkumar.mathur@und.edu

Abstract

Foxp3$^+$ regulatory T cells (Tregs) maintain immune homeostasis, yet the process that preserves their stability during aging remain unclear. Mechanistic progress has been hindered by models that ablate Tregs or delete *Foxp3*, which induce acute autoimmunity and prevent longitudinal study of physiological regulatory drift. Here, we establish a dose-dependent mitochondrial framework that preserves Treg lineage survival while permitting gradual metabolic attenuation. Using Treg-restricted TFAM modulation, a complementary haploinsufficient model, and whole-spleen single-cell profiling. We identify lineage-selective immune remodeling characterized by contraction of naïve CD8$^+$ and follicular B-cell pools, alteration of CD4$^+$ states, expansion of activated Tregs, and emergence of neuroimmune stress linked transcriptional modules that parallel physiological aging. Mechanistically, mitochondrial insufficiency is associated with functional loss of *FOXP3*-centered chromatin coordination and enrichment of NF-κB/NFAT/AP-1 inflammatory and senescence programs while lineage identity remains detectable. Partial mitochondrial attenuation within Tregs alone is sufficient to drive chronic low-grade systemic inflammation, neuromuscular decline, gut microbial restructuring, and elevated microglial responsiveness without Treg depletion. Pharmacologic and microbiota-directed interventions partially reduce inflammatory tone and improve functional metrics. Together, our findings identify TFAM as a key regulator of immune aging and reveal that healthy mitochondrial function in Tregs is essential for protecting against inflammaging and age-associated functional decline.

Introduction

Immune aging is increasingly defined by dysregulated inflammatory tone instead of a uniform reduction in leukocyte counts[1, 2, 3, 4]. Converging evidence from human cohorts and murine models indicates that subtle cytokine elevation, redistribution of lymphoid subsets, and gradual functional drift occur prior to the manifestation of overt immunodeficiency, suggesting that the aging immune system is actively recalibrated rather than passively depleted. The gradual increase of long-lasting, low-grade inflammation is often called inflammaging which reflects disturbed immune balance rather than loss of immune cells, suggesting that regulatory pathways remain present but slowly change in function over time.

Foxp3$^+$ regulatory T cells are a metabolically and transcriptionally distinct lineage that rises predominantly within the CD4$^+$ T cell compartment and enforce peripheral tolerance and suppress immunopathology[5, 6, 7, 8, 9]. In contrast, conventional effector T cells promote inflammation and primarily utilize glycolysis to support clonal expansion[10, 11]. The metabolic state of Tregs influences

their epigenetic landscape, particularly at the conserved non-coding sequence 2 (CNS2) enhancer of the Foxp3 gene. Oxidative phosphorylation (OXPHOS) and fatty acid oxidation (FAO) support the maintenance of an open chromatin configuration at CNS2, facilitating sustained Foxp3 expression[12, 13, 14, 15]. This epigenetic regulation is essential for preserving Treg identity and suppressive function. Disruption of mitochondrial metabolism in Tregs can lead to decreased *Foxp3* expression and increased susceptibility to acquisition of effector-like programs. Specifically, impaired OXPHOS and FAO may result in the upregulation of transcription factors such as T-bet (TBX21), RORγt (RORC), and IRF4, which are associated with effector T cell lineages. This shift undermines Treg stability and promotes inflammatory responses. Emerging evidence, including from our own investigations, supports the concept that mitochondrial dysfunction is not merely correlative, but acts as a proximal driver of Treg instability, fueling systemic inflammation and age-associated immune remodeling[12, 16, 17, 18]. Progress in dissecting these mechanisms has been constrained by experimental systems that eliminate Tregs entirely, including scurfy mutations and diphtheria-toxin based *Foxp3* depletion models, which provoke rapid systemic autoimmunity and early lethality [19, 20, 21]. Although these approaches firmly establish the necessity of *Foxp3* immune tolerance, they do not reproduce the gradual metabolic and transcriptional drift observed in physiological aging, where peripheral mature Tregs persist but slowly alter function. As a result, distinguishing intrinsic regulatory adaptation from secondary inflammatory collapse has remained challenging.

In recent years, mitochondrial genome integrity has emerged as an intrinsic checkpoint linking cellular metabolism to immune longevity[9, 22, 23]. Mitochondrial transcription factor A (TFAM), a nuclear-encoded high-mobility group (HMG) protein, is crucial for maintaining mitochondrial DNA (mtDNA) integrity and regulating redox homeostasis[24, 25]. Beyond its structural role in mtDNA packaging, TFAM modulates electron transport chain (ETC) function and limits mitochondrial reactive oxygen species (ROS) production. Loss of TFAM expression leads to mtDNA depletion, destabilization of oxidative phosphorylation (OXPHOS) complexes (CI-CIV), and activation of mitonuclear stress responses These include the mitochondrial unfolded protein response (UPR^{mt}), integrated stress response (ISR) via ATF4/DDIT3, and downstream inflammatory signaling involving NF-κB and STAT1[25, 26, 27, 28]. The mitochondrial stress responses influence chromatin and transcriptional regulators, including histone deacetylases (HDACs), SIRT1, ten-eleven translocation (TET) enzymes, and polycomb repressive complex 2 (PRC2) components like EZH2. These regulators, which modulate histone acetylation/methylation and DNA demethylation states, are critical for *Foxp3* expression and the fidelity of the Treg lineage. Thus,

103 redox-sensitive epigenetic rewiring under mitochondrial stress may mechanistically compromise
104 Treg stability and function. However, whether TFAM-dependent mitochondrial integrity operates
105 as an upstream checkpoint safeguarding immune homeostasis remains an unresolved question.
106
107 Interestingly, *Tfam* disruption in $CD4^+$ T-cell compartment has been shown to accelerate systemic
108 inflammation and tissue decline[17]. Prior studies employing Foxp3-directed TFAM deletion further
109 demonstrate that mitochondrial impairment in regulatory T cells can precipitate acute
110 inflammatory pathology or alter tumor progression[12, 16]. However, whether declining mitochondrial
111 integrity confined specifically to *Foxp3*$^+$ Tregs is sufficient to reorganize whole-immune
112 architecture toward an aging-like trajectory rather than merely reproducing inflammatory
113 syndromes associated with overt regulatory dysfunction has remained unclear. Our single-cell
114 transcriptomic analyses revealed that *FOXP3*$^+$ T cells exhibit mitochondrial stress–associated
115 signatures that track with inflammatory skewing in human aging and frailty, implicating
116 mitochondrial dysfunction in progressive immune remodeling[18]. Consistent patterns reported in
117 independent cohorts further strengthen the association between mitochondrial perturbation and
118 age-related shifts in Treg state and function[30, 31, 32, 29]. Collectively, these single-cell studies
119 suggest that early mitochondrial dysfunction could involve in the gradual re-shaping of immune
120 trajectories.
121
122 Here, to dissect this relationship, we employed two Treg-specific TFAM mouse models: a
123 conditional knockout ($Foxp3^{+cre}Tfam^{fl/fl}$) and a heterozygous model ($Foxp3^{+cre}Tfam^{f/+)}$, which
124 exhibits a moderate physiological reduction in TFAM expression. Together, these models
125 recapitulate aspects of the progressive mitochondrial decline observed during both normal and
126 pathological aging. Mitochondrial dysfunction in the Treg lineage led to a cascade of
127 immunological issues, including hyper-inflammatory $CD4^+$ T cell fate changes and altered gene
128 expression. Such shifts are consistent with hallmarks of inflammaging, which include chronic low-
129 grade inflammation, gut microbial dysbiosis, and neuroimmune activation. Together, our study
130 establishes a scalable experimental framework to directly examine how gradual mitochondrial
131 decline in persistent Tregs alters systemic inflammatory set-points. Our findings establish
132 mitochondrial integrity not only as a metabolic feature but also as a modifiable regulator of Treg
133 quality and immune homeostasis, highlighting mitochondrial maintenance as a potential avenue
134 to mitigate chronic age-associated inflammation.
135
136 **Results**

137 **Treg-intrinsic TFAM loss in Foxp3$^+$ Tregs reprograms CD4$^+$ T cell lineage trajectories and**
138 **enforces effector bias**
139 To investigate how mitochondrial TFAM deficiency in *Foxp3$^+$* Tregs perturb systemic CD4$^+$ T cell
140 homeostasis, we conducted single-cell RNA sequencing (scRNA-seq) on whole spleens from
141 Foxp3^{Cre}Tfam$^{f/f}$ (TFAM cKO) and Tfam$^{f/f}$ (wild-type) (Fig. 1A). This model selectively impairs
142 mitochondrial DNA maintenance in mature Tregs while largely preserving Foxp3 expression and
143 lineage presence, enabling assessment of regulatory *functional* dysfunction rather than the
144 severe autoimmune phenotypes produced by Foxp3-null/scurfy or diphtheria-toxin depletion
145 systems [19, 20, 21]. Following stringent quality control, we retained transcriptomic profiles from
146 14,198 cells in TFAM cKO and 34,958 cells in wild-type mice, excluding erythroid lineage cells
147 from downstream analyses (Fig. 1B). Based on canonical immune markers, we resolved 21 major
148 immune subsets across 26 transcriptionally distinct clusters conserved across both genotypes
149 (Fig. 1B; Fig. S1A-C). Notably, naïve-associated CD8$^+$ T cells marked by Tcf7 and Lef1 were
150 reduced, as were follicular B-cell populations expressing Cd79b and Fcer2a, whereas total CD4$^+$
151 abundance remained relatively stable but underwent pronounced transcriptional redistribution.
152 Importantly, the contraction of naïve CD8$^+$ cells was not interpreted as direct mitochondrial
153 impairment within CD8$^+$ cells, but rather as a secondary consequence of altered regulatory set-
154 points consistent with physiological immune aging in which naïve CD8$^+$ attrition is a prominent
155 and early feature of compartmental drift [1, 2].
156
157 TFAM deletion in Tregs elicited a striking inflammatory reprogramming of the CD4$^+$ T cell
158 compartment, marked by enrichment of TNF signaling, inflammation-associated aging pathways,
159 and gene signatures linked to tumorigenic transformation (Fig. S1D; Table S1). Upregulation of
160 pro-inflammatory mediators including *S100a6* and *Zfp3612*, coupled with diminished expression
161 of homeostatic regulators such as *Cd79b* and *Fcer2a*, was consistent with premature immune
162 aging (Fig. S1E). To examine how TFAM-deficient Tregs influence CD4$^+$ T cell diversity at a
163 steady state, we profiled subset heterogeneity based on canonical markers. Based on canonical
164 lineage-defining markers, six transcriptionally defined CD4$^+$ T cell subsets were identified: naïve
165 (*Sell, Lef1, Tcf7*), effector memory (TEM; *S100a4, S100a6*), exhausted (*Tnfsf8, Tbc1d4*),
166 conventional Tregs (nTregs; *Ikzf2, Il2ra, Cd74*), activated Tregs (aTregs; *Icos, Rgs1*), and
167 cytotoxic CD4$^+$ T cells (*Ccl5, Gzma, Gzmb*) (Fig. 1C, D). Comparative analysis revealed
168 substantial shifts in subset proportions in TFAM cKO mice (Fig. 1E, Fig. S2A), including marked
169 expansion of aTregs (+105.6%), cytotoxic CD4$^+$ T cells (+250.3%), and TEM cells (+208.4%),
170 alongside reduced frequencies of exhausted (-25.4%) and naïve (-29.8%) subsets, and a modest

171 reduction in nTregs (-6.4%). These shifts reflect an altered balance favoring pro-inflammatory and
172 terminally differentiated effector states. Thus, TFAM attenuation preserved lineage identity but
173 reshaped qualitative fate composition, aligning with aging datasets in which Tregs persist yet
174 adopt activated, cytokine-responsive phenotypes rather than disappearing [30, 31].
175
176 To gain mechanistic insights into these phenotypic alterations, differential gene expression and
177 pathway enrichment analyses in $CD4^+$ T cells from TFAM cKO versus WT mice uncovered strong
178 upregulation of TNFα signaling, calcium flux, and cytokine/chemokine networks, with concurrent
179 downregulation of hematopoietic lineage maintenance programs (Fig. 1F, Fig. S2B, Table S2).
180 IL-17 signaling was particularly enriched across TEM, exhausted, aTregs, and nTregs, suggesting
181 a bias toward pro-inflammatory Th17-like conversion a hallmark of increased Treg plasticity.
182 Recognizing that $CD4^+$ T cell diversity is governed by dynamic lineage trajectories, we next
183 applied trajectory inference to map differentiation states and fate decisions within $CD4^+$ T cell
184 compartments. Trajectory inference using Monocle revealed a branched differentiation
185 architecture with three bifurcation points and two dominant paths (P1 and P2), covering seven
186 transcriptional states (Fig. 1G-I, Fig. S2C-D). $CD4^+$ T cells from WT mice primarily followed the
187 P1 trajectory, occupying States 4-6, whereas TFAM cKO cells were enriched in States 1, 2, and
188 6, indicating a skewing toward the P2 trajectory and altered fate commitment. Naïve T cells, while
189 concentrated in States 4-6 in both groups, were aberrantly distributed across States 1, 2, and 7
190 in cKO mice. Notably, aTregs were enriched in State 1, while cytotoxic $CD4^+$ T cells were depleted
191 in terminal States 1 and 7 (Fig. 1I). The shifts point to preferential lineage commitment along the
192 alternative P2 trajectory in TFAM-deficient cells, contrasting with the homeostatic P1 path favored
193 by wild-type counterparts. Next, we applied RNA velocity analysis to confirm the inferred
194 directionality of fate transitions, supporting Monocle-inferred pseudotime dynamics (Fig. 1J).
195 Gene expression kinetics along pseudotime identified four temporally distinct clusters. Early
196 expressed Cluster 1 genes (*Klf3, Sell, Bcl2, Satb1*) were enriched in hematopoietic progenitors,
197 while Cluster 2 genes (*Anxa2, S100a4, Ccl5, S100a6, Lgals1*) were associated with terminal
198 effector differentiation and inflammation (Fig. 1K). Strikingly, Cluster 2 was enriched for gene
199 signatures linked to neurodegenerative diseases, Alzheimer's, Parkinson's, and ALS, as well as
200 oxidative phosphorylation (Fig. 1K, Table S3). KEGG analysis across Monocle states further
201 demonstrated that State 1, enriched in TFAM-deficient cells, was associated with
202 neuroinflammatory and neurodegeneration-related programs, whereas hematopoietic renewal
203 pathways dominated the WT-favored P1 trajectory (Fig. 1K, Fig. S2D, Table S4). These findings
204 suggest that Treg mitochondrial dysfunction promotes effector $CD4^+$ T cell programs enriched for

205 transcriptional features observed in neuroinflammatory and neurodegenerative conditions. Flow
206 cytometry confirmed the expansion of $CD4^{+}CD44^{hi}CD62L^{lo}$ effector T cells and depletion of
207 $CD4^{+}CD44^{lo}CD62L^{hi}$ naïve populations in secondary lymphoid organs of TFAM cKO mice (Fig.
208 1L-M). Functionally, TFAM-deficient Tregs exhibited reduced suppressive capacity, allowing for
209 enhanced proliferation of wild-type responder $CD4^{+}$ T cells in co-culture assays (Fig. 1N).
210 Collectively, these findings indicate that mitochondrial transcriptional attenuation restricted to
211 $Foxp3^{+}$ Tregs associates with coordinated splenic immune remodeling characterized by naïve
212 $CD8^{+}$ contraction, follicular B-cell reduction, diversification of $CD4^{+}$ states, selective expansion of
213 $ICOS^{+}$ activated Tregs, and enrichment of stress- and IL-17–linked transcriptional programs. In
214 aggregate, the resulting immune landscape aligns with aging-like immune drift redistribution and
215 functional reprogramming across compartments rather than a depletion-equivalent phenotype or
216 synchronized effector expansion typical of acute Treg ablation.
217
218 **TFAM loss in Tregs unleashes a multi-lineage stress response coupled with inflammatory**
219 **and senescence signatures**
220 To investigate how mitochondrial TFAM deficiency disrupts transcriptional networks in $Foxp3^{+}$
221 Tregs, particularly those governing inflammation-associated regulons and downstream TNF-
222 driven signaling implicated in Treg destabilization and effector skewing of $CD4^{+}$ T cells, we
223 performed gene regulatory network (GRN) inference using scRNA-seq data from TFAM cKO and
224 wild-type spleens. We identified 177 high-confidence regulons distributed across $CD4^{+}$ T cell
225 subsets (Fig. 2A). Canonical immunoregulatory transcription factors, including *Irf2, Irf8, Irf9,* and
226 *Bcl11a*, were preferentially enriched in wild-type Tregs, reflecting preservation of suppressive
227 lineage identity. In contrast, TFAM-deficient Tregs showed marked activation of inflammatory
228 regulons such as *Nfkb2, Nfatc1, Rora,* and *Runx2*, consistent with a breach in the mitochondrial
229 checkpoint that permits effector conversion (Fig. 2A, Fig. S3). Stress-adaptive regulons, including
230 *Egr1, Junb,* and *Xbp1*, were enriched in exhausted T cells, aTregs, and even nTregs in TFAM
231 cKO mice, pointing to a convergent transcriptional stress response. Enrichment of *Runx3* in
232 cytotoxic $CD4^{+}$ subsets further highlighted mitochondrial TFAM as a key repressor of cytolytic
233 plasticity. Notably, upregulation of *Ddit3* across all $CD4^{+}$ subsets indicated a shared mitochondrial
234 stress program (Fig. 2A). Targeted expression profiling of inflammatory regulators, including
235 *Prdm1, Nfkb1, Nfkb2,* and *Ahr*, showed strong induction in TFAM-deficient Tregs, reinforcing the
236 destabilization of the regulatory axis (Fig. 2B). The ensuing Systemic inflammation further
237 activates myeloid-derived cells, such as monocytes and macrophages, enhancing their oxidative
238 phosphorylation activity. This heightened metabolic state contributes to increased

239 neuroinflammation, and the activation of neurodegenerative pathways associated with
240 Parkinson's and Alzheimer's diseases (Fig. 2C). To assess downstream consequences, bulk
241 RNA-seq of TFAM cKO splenocytes revealed strong induction of cell death pathways, including
242 apoptosis and necroptosis (Fig. 2D). Immunoblotting confirmed caspase-3 and -8 cleavage, IκBα
243 degradation, and phosphorylation of RIPK1, RIPK3, and MLKL signatures of RIPK-mediated
244 immunogenic cell death (Fig. 2E). This was substantiated in situ by Annexin V/PI staining, which
245 revealed marked increases in apoptotic and necroptotic cell populations in both splenic and
246 cutaneous tissues (Fig. S4E), indicating systemic cytopathology secondary to mitochondrial
247 collapse in Tregs. Collectively, these findings lend support to regulatory destabilization caused by
248 chronic inflammatory injury rather than wholesale Treg lineage elimination.
249
250 To determine if Treg-specific mitochondrial dysfunction initiates systemic decline, we monitored
251 TFAM cKO mice longitudinally. While born at Mendelian ratios, these mice developed progressive
252 organismal deterioration from 4 weeks, including alopecia, kyphosis, lymphoid organomegaly,
253 impaired mobility, and early mortality ($p<0.0001$; Fig. S4A-B). By 8-10 weeks, they developed
254 severe skeletal muscle atrophy, adipose tissue loss, cortical bone thinning, and markedly reduced
255 survival relative to wild-type littermates (Fig. S4C). Histological analysis revealed inflammatory
256 infiltration in the lung, liver, colon, and kidney (Fig. 2F, S5A), and cortical bone loss (Fig. 2F, 2G).
257 Spleens from TFAM cKO mice exhibited splenomegaly, marginal zone disruption, and follicular
258 disorganization (Fig. 2H). These phenotypes were consistent with disrupted immune regulation
259 downstream of Treg-intrinsic mitochondrial dysfunction. Mitospy analysis showed mitochondrial
260 depolarization and increased oxidative stress in cKO Tregs (Fig. 2I, Fig. S4D, S4E). Multiplex
261 cytokine profiling revealed a pronounced pro-inflammatory signature characterized by elevated
262 levels of IL-17, IFN-γ, IL-12, IFN-β, GM-CSF, and IL-27, in parallel with significantly increased
263 circulating TNF-α and IL-6, reflecting systemic immune activation and inflammatory amplification
264 (Fig. 2J; Fig. S5B). At the molecular level, cKO mice exhibited upregulation of *Cdkn2a (p16)* and
265 *Cdkn1a (p21)* (Fig. 2K), and immunoblots confirmed elevated p53, CDK4, p16, and p21 (Fig. 2L),
266 indicative of a senescence-like program. Whole-spleen RNA-seq revealed enrichment of
267 inflammatory and aging-related networks (Fig. 2M). Gene Set Enrichment Analysis (GSEA) from
268 spleen, skin and brain revealed enrichment of neuroactive signaling, circadian disruption, and
269 protein trafficking defects pathways associated with immune aging and systemic decline (Fig. 2N,
270 Table S5). These findings establish TFAM as a critical mitochondrial checkpoint that safeguards
271 Treg identity, restrains inflammation, and maintains immune equilibrium.

272 **Partial TFAM reduction in Tregs as a critical driver of aging pathologies,**
273 **neuroinflammation, and cognitive decline**
274 To model the progressive mitochondrial decline characteristic of physiological aging, we
275 transitioned to a Treg-specific TFAM heterozygous mouse (TFAM Het; *Foxp3*^{Cre}*TFAM*$^{f/+}$). While
276 complete TFAM ablation in Tregs provides mechanistic insight into the necessity of mitochondrial
277 integrity for immune homeostasis, the rapid-onset pathology of this model precludes longitudinal
278 interrogation of chronic immune aging and neurodegenerative processes. To better understand,
279 the TFAM Het model, where one functional allele of the *Tfam* gene is deleted specifically in
280 CD4$^+$Foxp3$^+$ Tregs, resulting in a sustained ~50% reduction in TFAM expression in CD4$^+$Foxp3$^+$
281 Tregs. This genetically defined model recapitulates subclinical mitochondrial insufficiency and
282 mirrors the progressive mitochondrial decline characteristic of the human aging trajectory.
283 Supporting its translational relevance, analysis of human PBMC transcriptomes revealed a
284 significant age-dependent decline in TFAM expression, reinforcing its role as a mitochondrial-
285 immune rheostat (Fig. 3A). By 8-10 months, TFAM Het mice exhibited classic hallmarks of aging,
286 including kyphosis, weight loss, and reproductive decline (Fig. 3B-C, Fig. S6A-B).
287
288 Histopathological evaluation demonstrated that 8-month-old TFAM cKO mice exhibited
289 pronounced structural degeneration in the spleen and lung, markedly exceeding that observed in
290 both 8-week-old controls and TFAM Het counterparts. Notably, the extent of tissue deterioration
291 in TFAM-deficient mice phenocopied the age-associated pathology typically seen in 2-year-old
292 wild-type mice, underscoring the accelerated aging phenotype driven by Treg-intrinsic
293 mitochondrial dysfunction (Fig. S6C). Senescence markers *Cdkn2a (p16*^{Ink4a}*)* and *Cdkn1a*
294 *(p21*^{Cip1}*)* were significantly upregulated in splenic CD4$^+$ T cells (Fig. 3D), implicating mitochondrial
295 stress induced senescence. Circulating TNF-α and IL-6 levels were markedly elevated (Fig. 3E),
296 indicative of persistent low-grade inflammation. Neuromuscular evaluation revealed diminished
297 grip strength (Fig. 3F), and behavioral assays demonstrated reduced exploratory activity and
298 locomotor hypoactivity (Fig. 3G), consistent with CNS dysfunction. To interrogate the
299 neuroanatomical consequences of peripheral Treg mitochondrial instability, cresyl violet staining
300 of brain sections revealed substantial neuronal loss in the hippocampus and cortex of 8-month-
301 old TFAM Het mice relative to 8-week counterparts (Fig. 3H-I). PCA plots from longitudinal
302 hippocampal RNA-seq profiling revealed a clear difference between Het8M group (T) and Het 8W
303 group (Y) (Fig. 3J), Notably, compared to both 8-week-old wild-type and age-matched 8-month-
304 old controls we observed marked upregulation of neural stress–associated genes including
305 *Gabra5*, *Slc38a5*, *Calcr*, and *Ganbare* (Fig. 3K). Further compared to wild 8W and comparable

306 8M TFAM Het mice shown KEGG pathway enrichment shown a marked elevated, inflammatory
307 signaling, Garabergic synapses neuro-active-ligand-receptor interaction and neurodegeneration-
308 linked pathways (Fig. 3L). To validate the functional relevance of these molecular changes, we
309 next assessed neuroimmune phenotypes at the cellular level. Iba1 immunohistochemistry
310 revealed widespread activation of amoeboid microglia in TFAM Het brains (Fig. 4A-B), with NeuN
311 co-staining confirming adjacent neuronal loss. Flow cytometric analysis revealed elevated MHC-
312 I expression on brain-resident $CX3CR1^+$ microglia in late-phase TFAM Het mice (Fig. 4C),
313 indicating enhanced antigen presentation. Upon TNF-α stimulation, purified $CX3CR1^+$ microglia
314 from TFAM Het mice exhibited increased expression of IL-1β, TNFR1, and IL-6 transcripts,
315 highlighting a heightened sensitivity to TNF-driven inflammatory activation compared to WT
316 controls (Fig. 4C-D). These findings collectively support a peripheral-to-central immunometabolic
317 cascade, wherein Treg-intrinsic mitochondrial insufficiency initiates systemic inflammation,
318 senescence, and CNS immune activation. The TFAM Het model reveals that gradual
319 mitochondrial decline in $CD4^+$ Tregs is sufficient to disrupt systemic immune homeostasis,
320 propagate neuroinflammation, and accelerate degenerative aging processes.
321
322 **TFAM insufficiency in Tregs drives microbiota-lipid dysregulation and neuroinflammatory**
323 **reprogramming via the gut-brain-immune axis**
324 Mitochondrial metabolism in immune cells is closely coupled to host lipid flux and microbiota-
325 derived metabolites[32]. We showed that advancing age is accompanied by progressive
326 dysregulation of host–microbial interactions, forming a bidirectional cycle linking metabolism,
327 microbial composition, and immune regulation[33]. Recently CD4 T cell therapy shown counteracts
328 inflammaging and senescence by preserving gut barrier integrity[34]. We therefore asked whether
329 gradual TFAM reduction within regulatory T cells also alters the intestinal metabolic environment
330 and downstream immune tone. Stable Treg identity depends on intact oxidative metabolism.
331 Short-chain fatty acids (SCFAs), especially butyrate and propionate, reinforce FOXP3 expression
332 through mitochondrial–epigenetic coupling[35, 36, 37]. It has remained unclear whether long-lived
333 Tregs undergoing slow mitochondrial decline can influence microbial ecology. Using a graded
334 TFAM-insufficiency strategy that preserves lineage survival while attenuating mitochondrial
335 transcription, and applying longitudinal 16S sequencing using our previously published protocol
336 in aging mouse model [33], we observed progressive, age-associated restructuring of gut microbial
337 communities in TFAM Het mice (Fig. 5A–B). Beta-diversity analyses separated groups by both
338 genotype and age (Fig. 5B). This pattern indicates gradual community redirection rather than
339 abrupt dysbiosis. At the phylum level, aged TFAM Het animals showed relative expansion of

340 Campylobacterota and contraction of Bacteroidota (Fig. 5C). Shared-taxa analysis revealed a
341 preserved core microbiota across age-matched groups (Fig. 5D). This overlap suggests that these
342 specific bacterial changes are associated with aging processes common to both genotypes,
343 highlighting potential age-related microbial shifts that occur irrespective of TFAM status.
344
345 Notably, differential abundance analysis identified 18 aging-associated microbial taxa altered
346 across genotypes, including the depletion of canonical SCFA-producing lineages, such as
347 *Lactobacillus murinus*, *Odoribacter*, and *Prevotellaceae_UCG-001* (Fig. 5E). Given that SCFAs
348 like butyrate are critical for Treg stability, intestinal barrier integrity, and peripheral immune
349 tolerance, these compositional shifts suggest a collapse in microbial-derived immunoregulatory
350 tone. To further contextualize these compositional alterations, we performed KEGG-based
351 predictive metagenomic analyses to infer functional capacities of the microbial communities. In 8-
352 month-old mice, predicted microbial gene modules were enriched for KEGG pathway annotations
353 broadly associated with aging- and immune-related processes, including longevity regulation,
354 RIG-I–like receptor signaling, FoxO signaling, MAPK signaling, and endocannabinoid-associated
355 pathways, relative to 8-week-old controls (Fig. 5F). Importantly, these annotations reflect
356 predicted microbial functional potential rather than direct activation of corresponding host
357 endogenous pathways. Within this framework, lipid metabolism emerged as a particularly
358 disrupted node to regulate Treg stability, with significant alterations in pathways governing
359 unsaturated fatty acid biosynthesis [36, 38, 39, 40, 41, 42, 43]. In TFAM Het mice, lipid metabolism was
360 profoundly disrupted, with significant alterations observed in pathways governing unsaturated
361 fatty acid biosynthesis, PI3K-Akt signaling, spinocerebellar ataxia pathways, sphingolipid
362 metabolism, primary bile acid biosynthesis, and fatty acid degradation (Fig. 5G). Concurrently,
363 neurotransmission-related pathways, including GABAergic and glutamatergic synapses, were
364 markedly downregulated in aged TFAM Het mice (Fig. 5G). This downregulation aligns with
365 observed behavioral dysfunction and hippocampal atrophy in 8-month-old TFAM Het mice (Fig
366 3H, 3I, 4A). These findings support a model wherein mitochondrial impairment in regulatory T
367 cells perturbs microbial generation of neuromodulator metabolites, disrupting gut-brain signaling
368 and predisposing the central nervous system to inflammatory remodeling[44, 45, 46, 47].
369
370 To mechanistically link microbial changes with host gene regulation, we performed an integrated
371 correlation analysis between differentially abundant bacterial taxa and host transcriptomes
372 obtained from brain. This analysis uncovered 323 significant microbiota-host gene interactions
373 (FDR-adjusted p <0.05), mapping a complex regulatory network that bridges microbial

374 composition and neuroimmune signaling (Fig. 5H). *Helicobacter* species exhibited a strong
375 positive correlation with *Ntsr2*, a neurotensin receptor involved in both neurotransmission and
376 microglial activation, suggesting microbial influence over neural inflammatory circuits.
377 *Lactobacillus* emerged as a central node, negatively correlating with neuroendocrine transcripts
378 (*Pomc*, *Sstr5*, *Ntsr2*) and neuronal developmental regulators (*Elk3*, *Sox4*), while positively
379 correlating with inflammatory mediators (*Sele*, *Mpo*, *Ifitm6*), linking its depletion to neuroimmune
380 destabilization. *Lachnospiraceae_NK4A136_group* was associated with complement-mediated
381 inflammation, showing a positive correlation with *C5ar2* and negative regulation of *Sstr5* and *Elk3*,
382 reinforcing its role in shaping neuroinflammatory tone. To assess downstream inflammatory
383 consequences associated with microbiota-linked alterations in TFAM Het mice, we quantified
384 inflammatory cytokine transcripts in peripheral tissues. IL-1β and TNFR1 expression were
385 significantly elevated in brain tissue (Fig. 5I), indicating the presence of sustained, low-grade
386 neuroinflammatory signaling. These inflammatory changes occurred in concert with marked shifts
387 in microbial community composition and predicted microbial metabolic capacity, including
388 pathways related to lipid and SCFA-associated processes. Together with concurrent shifts in
389 microbial composition and predicted metabolic capacity, these findings support a model in which
390 partial TFAM insufficiency in regulatory T cells destabilizes immune homeostasis and increases
391 susceptibility to age-associated systemic and neuroinflammatory remodeling.
392
393 **Modulation of mitochondrial stress pathways attenuates systemic inflammation and**
394 **aging-associated pathology**
395 To determine whether immune pathology associated with Treg-specific TFAM deficiency is
396 amenable to intervention, we evaluated resveratrol (RSV) treatment in TFAM cKO mice. RSV is
397 a pleiotropic SIRT1-associated compound with established effects on cellular stress responses
398 and inflammatory signaling. Prior studies have demonstrated that the protective effects of RSV
399 across multiple disease contexts are mediated, at least in part, through activation of the PGC-1α–
400 NRF-1–TFAM axis, thereby promoting mitochondrial biogenesis and transcriptional capacity in a
401 SIRT1-dependent manner[48, 49]. Accordingly, RSV was administered intraperitoneally at 7 mg/kg
402 every other day for four weeks (Fig. 6A). Consistent with these reports, RSV treatment was
403 associated with increased transcript levels of *PGC-1α*, *PGC-1β*, and the mitochondrial
404 transcription factors *TFAM* and *TFB2M*, indicating engagement of mitochondrial biogenic
405 programs. At the tissue level, RSV treatment was associated with altered mitochondrial
406 membrane potential, as reflected by MitoSpy staining in skin sections (Fig. 6B), and coincided
407 with a marked reduction in systemic inflammatory burden, evidenced by decreased circulating

408 TNF-α and IL-6 levels (Fig. 6C). In parallel, expression of senescence-associated genes *Cdkn2a*
409 ($p16^{Ink4a}$) and *Cdkn1a* ($p21^{Cip1}$) in splenocytes was reduced, consistent with attenuation of
410 inflammation-linked senescence programs (Fig. 6D-F). Histopathological analysis further
411 revealed diminished inflammatory infiltration and improved preservation of tissue architecture in
412 lungs, liver, and kidney (Fig. 6G).
413
414 Treg stability is also influenced by microbiota-derived metabolites, especially short-chain fatty
415 acids that support oxidative metabolism and chromatin accessibility at the *Foxp3* locus [16, 30, 36, 41,
416 43]. We therefore evaluated whether environmental metabolic inputs show similar corrective trends.
417 Fecal microbiota transplantation (FMT) was performed in TFAM heterozygous (TFAM Het) mice,
418 which exhibit a gradual, non-lethal phenotype more consistent with physiological immune aging
419 than the acute TFAM cKO model. Because regulatory T cell function and peripheral immune tone
420 are strongly influenced by microbiota-derived signals, we reasoned that partial TFAM insufficiency
421 may lower the threshold for microbiota-dependent modulation of host physiology. Antibiotic-
422 conditioned TFAM Het mice received fecal material from TFAM-sufficient donors over three days,
423 followed by a three-week recovery period (Fig. 6H). FMT was associated with improved
424 neuromuscular performance, including increased rotarod endurance and enhanced forelimb grip
425 strength (Fig. 6I). The observed functional improvements indicate that TFAM insufficiency renders
426 host physiology responsive to microbiota-dependent modulation. Together, pharmacologic and
427 microbiota-directed interventions collectively suggest that TFAM-linked mitochondrial
428 competence in Tregs serves as a modifiable nexus linking cellular bioenergetics, immune
429 modulation, and organismal aging. These results align with the perspective that mitochondrial and
430 metabolic support can mitigate the inflammatory and functional aspects of immune aging, rather
431 than effecting a conclusive reversal (Fig. 6J).
432
433 **Discussion**
434 The progressive decline in mitochondrial transcriptional integrity is a hallmark of aging, yet its
435 direct impact on immune regulation and cellular fate remains insufficiently characterized[50, 51, 52 17,
436 32, 53]. Specifically, whether the decreasing mitochondrial transcriptional capacity within Tregs
437 directly initiates immune aging, or merely reflects broader senescent cues remain unresolved.
438 Here, we mechanistically establish TFAM as a central molecular rheostat of Treg identity and
439 systemic immune homeostasis. Using Treg-specific physiologically relevant graded TFAM
440 insufficiency, we demonstrate that progressive disruption of mitochondrial transcriptional output

441 rewires $CD4^+$ T cell fate, reshapes the gut microbial ecosystem, and primes the central nervous
442 system for neuroinflammatory remodeling.
443
444 A major limitation in immune aging research has been the absence of physiologically relevant
445 models that can selectively dissect the cell-intrinsic consequences of mitochondrial dysfunction
446 within Tregs across the aging trajectory. Existing models involving global TFAM deletion or tissue-
447 specific knockouts in high-turnover compartments often result in rapid lethality, systemic cytokine
448 storm, and developmental collapse, precluding longitudinal assessment of immune remodeling[12,
449 16, 24, 54, 55]. Similarly, Treg ablation models such as $Foxp3^{DTR}$ or DEREG mice induce severe
450 autoimmunity and fail to capture the progressive, transcriptionally encoded dysfunction of
451 suppressive Treg identity observed during physiological aging[19, 56]. Other aging models, including
452 $Ercc1^{-/\Delta}$, $BubR1^{H/H}$, and $Zmpste24^{-/-}$, reflect accelerated DNA repair defects or nuclear envelope
453 instability, but do not reproduce the slow, cell-specific decline in mitochondrial transcriptional
454 output characteristic of aging Tregs[57, 58,59].
455
456 To overcome these constraints, we developed the $Foxp3^{Cre}Tfam^{f/+}$ mouse, which induces a stable
457 ~50% reduction in TFAM within $Foxp3^+$ Tregs, consistent with the age-related TFAM decline
458 reported in human PBMCs. Unlike $Foxp3^{Cre}Tfam^{f/f}$ models that succumb to early mortality,
459 TFAMHet mice remain viable, thereby enabling longitudinal tracking of mitochondrial insufficiency
460 and its systemic consequences. With age, TFAMHet mice exhibit canonical features of
461 organismal aging kyphosis, sarcopenia, reproductive decline, and neuromuscular impairment
462 alongside immune aging hallmarks, including elevated $p16^{Ink4a}$, $p21^{Cip1}$, increased circulating IL-6
463 and TNF-α, and a shift of the $CD4^+$ T cell compartment toward $CD44^{hi}CD62L^{lo}$ effector memory
464 phenotypes. In the CNS, TFAMHet mice show heightened microglial activation ($CX3CR1^+$MHC-
465 I^{hi}) and hippocampal neuronal loss, consistent with peripheral-to-central immunometabolic
466 disruption (Fig. 3-4). Collectively, this model provides a genetically precise, temporally scalable
467 system to dissect how mitochondrial transcriptional fidelity in Tregs orchestrates immunological
468 aging, gut–brain communication, and tissue integrity. The TFAMHet mouse thus offers a tractable
469 platform for probing mitochondria-driven immunoregulation with translational relevance to human
470 aging.
471
472 While mitochondrial metabolism is known to sustain FOXP3 expression and Treg function, the
473 direct role of mitochondrial genome integrity specifically TFAM-dependent transcriptional control,
474 in orchestrating systemic $CD4^+$ T cell fate has remained undefined. As aging coincides with both

475 mitochondrial erosion and effector CD4$^+$ expansion, the mechanistic bridge linking these
476 processes has not been elucidated. By leveraging single-cell RNA sequencing spleens from
477 TFAMcKO mice, we uncover a profound reshaping of the CD4$^+$ T cell landscape. TFAM loss in
478 Tregs drives expansion of cytotoxic Gzmb$^+$Ccl5$^+$ subsets, S100a6$^+$ effector memory (TEM) cells,
479 and Icos$^+$Rgs1$^+$ aged-like Tregs (aTregs), coupled with depletion of early-stage Tcf7$^+$Lef1$^+$ naïve
480 and Tnfsf8$^+$ activated/exhaustion-associated populations. These alterations are consistent with
481 transcriptionally encoded, lineage-intrinsic reprogramming rather than being explained solely by
482 a secondary inflammatory milieu, as revealed by pseudotime reconstruction and RNA velocity
483 mapping. Notably, TFAM deficiency enforces commitment along an alternative P2 trajectory
484 enriched for neuroinflammatory and Th17-like gene modules, including *Anxa2*, *S100a4*, and *Ccl5*,
485 while repressing transcriptional brakes such as *Satb1* and *Bcl2*, suggesting a premature exit from
486 naïve states and loss of regulatory restraint. Mechanistic interrogation through gene regulatory
487 network (GRN) analysis reveals a collapse of Foxp3-lineage stability in TFAM-deficient Tregs,
488 marked by activation of inflammatory regulons (*Nfkb2*, *Nfatc1*, *Runx2*), cytolytic transcriptional
489 drivers (*Runx3*, *Prdm1*), and stress-response regulators (*Ddit3*, *Egr1*, *Junb*). The induction of
490 Ddit3, a hallmark of mitochondrial unfolded protein response (UPR^{mt}), together with
491 RIPK1/RIPK3/MLKL phosphorylation and caspase activation, is consistent with activation of
492 mitochondrial stress linked cell-death programs (including necroptosis and apoptotic
493 components) that could propagate paracrine stress to surrounding CD4+ subsets. This
494 remodeling is accompanied by transcriptional enrichment for neurodegenerative signatures,
495 including PI3K-Akt, FoxO, and oxidative phosphorylation pathways supporting a molecular link
496 between mitochondrial erosion in Tregs and CNS-relevant inflammatory programming. Our
497 findings delineate TFAM-dependent mitochondrial transcription as a master regulator of CD4$^+$ T
498 cell fate diversification, acting upstream of immunosenescence and neuroinflammation. By
499 defining mitochondrial instability in Tregs as a transcriptional checkpoint that governs effector
500 reprogramming, our study uncovers a novel axis of immune aging in which fidelity of Treg
501 mitochondrial transcription actively restrains the emergence of pro-inflammatory and potentially
502 neurotoxic CD4$^+$ states.
503
504 A central unresolved question in immunometabolism and aging is whether mitochondrial
505 dysfunction in Tregs actively shapes gut microbiota composition and influences the gut–brain
506 axis, or whether microbiome alterations are merely downstream byproducts of systemic aging[35,
507 36, 37]. While prior studies have established that SCFAs, particularly butyrate and propionate,
508 produced by gut microbiota promote FOXP3 expression and enhance Treg function through

509 epigenetic remodeling, the reciprocal influence of Treg mitochondrial state on microbial ecology
510 has remained mechanistically undefined[36, 41, 42, 43, 46]. Our study addresses this critical gap by
511 demonstrating that partial loss of mitochondrial transcriptional control in Tregs via TFAM
512 haploinsufficiency is sufficient to disrupt microbial-metabolite circuits essential for immune
513 regulation and neuroimmune integrity. In TFAMHet mice, we observed a marked depletion of
514 SCFA-producing bacterial taxa, including *Lactobacillus murinus* and *Odoribacter*, which are
515 essential for maintaining Treg epigenetic programming and FOXP3 stability[36, 44,60]. This dysbiosis
516 coincided with broad remodeling of gut lipid metabolic pathways, particularly involving bile acid
517 biosynthesis, sphingolipid metabolism, and signaling cascades such as PI3K-Akt and FoxO, that
518 are frequently implicated in aging-related immune and neuronal dysfunction[61, 62].
519
520 Importantly, our integrative analysis combining single-cell RNA-seq, lipidomics, microbiome
521 profiling, and host–microbiota transcriptome correlation revealed that Treg-intrinsic TFAM
522 insufficiency is associated with a systems-level disruption of gut–brain communication.
523 Neurotransmission pathways, especially GABAergic and glutamatergic circuits critical for CNS
524 function, were significantly disrupted in TFAMHet mice, aligning with hippocampal atrophy and
525 behavioral decline. Furthermore, correlation mapping uncovered 323 robust associations
526 between microbial taxa and neuroimmune gene networks. Notably, *Helicobacter* spp. positively
527 correlated with *Ntsr2*, a neurotensin receptor linked to microglial activation, while *Lactobacillus*
528 abundance negatively correlated with *Pomc*, *Sstr5*, *Ntsr2*, and transcriptional regulators *Elk3* and
529 *Sox4*, underscoring a microbial influence on CNS signaling cascades[41, 63]. Elevated expression
530 of inflammatory mediators such as *Il1β* and *Tnfr1* in TFAMHet tissues further support the
531 emergence of a chronic, low-grade inflammatory state driven by Treg mitochondrial insufficiency.
532 Recent studies have shown gut–brain axis is a complex, bidirectional communication network that
533 links the gastrointestinal tract and the central nervous system through neural, hormonal, and
534 immune pathways. Together, these findings support a previously underappreciated framework
535 linking Treg mitochondrial integrity with lipid-associated metabolic programs and microbial
536 community structure. In this model, Treg-specific TFAM insufficiency is associated with
537 coordinated changes in microbial composition, reduced representation of SCFA-producing taxa,
538 and heightened inflammatory signaling, reflecting a destabilized immunometabolic state. Rather
539 than defining a closed causal feedback circuit or a resolved gut-brain immune equilibrium, our
540 data position mitochondrial fidelity in Tregs as a critical stabilizing influence on immune–microbial
541 interactions that shapes susceptibility to systemic and neuroinflammatory remodeling during
542 aging.

543 Finally, we provide a proof-of-concept that mitochondrial dysfunction in Tregs is therapeutically
544 actionable through redox restoration and microbiome modulation. In the TFAMcKO model,
545 resveratrol an established activator of SIRT1 and PGC-1α signaling enhanced mitochondrial
546 biogenesis, restored mitochondrial membrane potential, reduced senescence markers, and
547 suppressed systemic inflammation. These findings align with prior reports demonstrating
548 resveratrol's capacity to improve mitochondrial function and mitigate age-associated inflammation
549 across tissues[49, 64]. In the chronic TFAM Het model, fecal microbiota transplantation (FMT)
550 restored SCFA-producing taxa, improved neuromuscular performance, and normalized immune
551 signatures. While FMT is increasingly recognized for its ability to modulate systemic immunity and
552 neurocognitive health via the gut-brain axis[65, 66], its role in regulating Treg mitochondrial function
553 remains poorly defined. Our data suggests that microbiota-derived metabolites may enhance
554 peripheral tolerance or indirectly support Treg mitochondrial homeostasis. Together, these
555 findings position Treg-intrinsic mitochondrial decline as a reversible driver of inflammaging and
556 support the translational potential of combining metabolic and microbial interventions to combat
557 age-related immune dysfunction (Fig. 6).
558
559 In sum, our study redefines Treg mitochondrial integrity as a central axis of immunological aging.
560 By uncovering TFAM as a lineage-specific molecular rheostat that governs immune suppression,
561 microbial composition, and neuroimmune resilience, we provide a unifying framework for the
562 mitochondrial regulation of systemic aging. These findings open translational opportunities for
563 mitochondria-targeted immunotherapies in chronic inflammatory diseases, neurodegeneration,
564 and age-associated immune decline.
565
566 **Methods**
567
568 **Animals**
569 Foxp3^{YFPCre} (Stock No: 016959) and TFAM$^{f/f}$ (Stock No: 026123) mice were obtained from
570 Jackson Laboratory (Bar Harbor, ME) and bred at the UND animal facility to create
571 Foxp3^{Cre}TFAM$^{f/f}$. All mice used in this study were from C57BL/6 backgrounds. Animals were kept
572 and bred in the UND Animal facility in a pathogen-free unit with a 12-hour light cycle, temperature,
573 and humidity control. Efforts are being made to reduce animal suffering and needless usage, in
574 accordance with the Institutional Animal Care and Use Committee's (IACUC) and National
575 Institutes of Health's Guide for the Care and Use of Laboratory Animals standards.
576 **Histology, immunohistochemistry, and acquisition of images**

577 Formalin-fixed, paraffin-embedded slices of various tissues were deparaffinized on slides using
578 xylene twice for 5 minutes each. Following that, they were switched to 100% ethanol twice for 3
579 minutes each and then to 95%, 75%, 65%, 50%, 35%, and 25% ethanol for 3 minutes each. Rinse
580 the slides for ten minutes under running tap water. The excess water was removed using a wiper
581 (KIMTECH SCIENCE) and 10% fetal bovine serum (FBS) in PBS was applied to the sections of
582 the slides and incubated for 30 minutes in the dark at room temperature (RT). FBS was gently
583 drained from the slides and cleaned with PBS (1X). MitoSpy (excitation (ex)/emission (em) at
584 577nm/598nm, MitoSpyTM Red CMXros (Cat#424801, BioLegend), After incubation, slides were
585 washed twice with 1X PBS and a single drop of mounting media (Fluoromount-G™ with DAPI,
586 Cat# 00-4958-02, Thermo Fisher Scientific) was applied to the tissue sections and the coverslip
587 was dipped into the mounting solution. For microglia ($IBA1^+$) and neuronal ($NeuN^+$)
588 immunostaining, mouse brains were fixed in 4% paraformaldehyde (PFA) in 1× PBS,
589 cryoprotected in 30% sucrose, and cryo-sectioned. Tissue sections were blocked in 0.2% Triton
590 X-100 and 5% normal goat serum in 1× PBS for 1 hour at room temperature, followed by
591 incubation with primary antibodies rabbit monoclonal anti-IBA1 (Cat# 17198, 1:1000) and mouse
592 monoclonal anti-Neuronal N (Cat# 94403, 1:1000) diluted in 0.2% Triton X-100 and 3% normal
593 goat serum in PBS for 24 hours at 4°C. After three 20-minute washes in PBS, sections were
594 incubated with appropriate secondary antibodies anti-Rabbit CF™594 antibody (Cat#
595 SAB4600107) and anti-mouse CF™488 antibody (Cat# SAB4600388) for 1 hour at room
596 temperature. Nuclei were counterstained using a single drop of Fluoromount-G™ with DAPI (Cat#
597 00-4958-02, Thermo Fisher Scientific) and sealed with nail polish. Fluorescence images were
598 acquired using a Leica Thunder Imaging System and an Olympus TIF fluorescence microscope.
599 Whole-slide histological scans were performed using a Hamamatsu NanoZoomer at the UND
600 Histology Core. Quantification of immunofluorescence signals was carried out using NIH ImageJ
601 software.
602
603 **Western blot**
604 Proteins were isolated from mouse tissue and/or single cells and homogenized in RIPA lysis
605 buffer containing a 1% protease inhibitor cocktail[67, 68, 69]. The protein concentration was
606 determined according to the manufacturer's instructions and our previously published protocol
607 using the Bio-Rad protein assay reagent. SDS-PAGE was used to extract a set quantity of cellular
608 protein and electroblotted onto an Immobilon-P transfer membrane (Cat# IPVH00010). The
609 immunological blot was blocked for 1 hour at room temperature with 5% nonfat dry milk in TBST
610 (25 mM Tris-HCL, pH 7.4, 1.5 M NaCl, 0.05% Tween-20), followed by overnight incubation with

611 primary antibodies at 4 °C. The next day, the membranes were washed five times at six-minute
612 intervals and incubated for one hour with HRP-conjugated secondary antibody (A16172,
613 Invitrogen) (1:1000) in 3% nonfat dry milk in TBST. The blots were then washed five further times
614 with TBST and developed with enhanced chemiluminescence. The following primary antibodies
615 were bought from Cell Signaling Technologies (Cell Signaling Technology, MA 01923, USA): RIP
616 (D94C12) Rabbit mAb #3493, MLKL (D2I6N) Rabbit monoclonal antibody #14993, RIPK3
617 (E1Z1D) Rabbit monoclonal antibody #13526, p-RIP (D1L3S) Rabbit monoclonal antibody
618 #65746, p-MLKL Rabbit monoclonal antibody (D6H3V) #91689, p-RIP3(D6W2T) Rabbit
619 monoclonal antibody #93654, p21 Waf1/Cip1 (12D1) rabbit monoclonal antibody #37543, p53
620 (1C12) Mouse monoclonal antibody #2524, CDK4 (D9G3E) Rabbit monoclonal antibody #12790,
621 PCNA (D3H8P) XP® Rabbit monoclonal antibody #13110, p16 INK4A (D3W8G) GAPDH
622 (D16H11) XP® Rabbit mAb #5174.
623
624 **RNA isolation and qPCR**
625 Total RNA was isolated from mouse tissues or single cells. The tissues were minced with a scissor
626 and added to 500 µL of TRIzol reagent (Ambion, cat# 15596018, Life Technologies, USA)[67, 68, 69].
627 A Fisher Scientific Sonic Dismembrator 100 was used to fully homogenize tissue solutions
628 (American Laboratory Trading, East Lyme, CT 06333. USA). The upper layer was removed, and
629 the RNA was precipitated with an equivalent volume of isopropanol and incubated at 55°C for 10
630 minutes before being resuspended in 50 µL of RNase-free water (Promega, Madison, WI, USA).
631 We determined the concentrations of RNA using a Smart-Spec plus spectrophotometer (Bio-
632 Rad). Then, using a High-Capacity cDNA Reverse Transcription Kit (Cat#: 4368814, Applied
633 Biosystem, Thermo Fisher Scientific), cDNA was generated from 0.5-1 µg of total RNA in a total
634 volume of 25 µL. The RT-PCR program was run for 5 minutes at 25 °C, 30 minutes at 42 °C, and
635 30 minutes at 95 °C. The cDNA templates were further diluted in water two-three times. For qPCR,
636 two microliters of diluted templates were utilized. A 96-well PCR plate (Cat#: MLL9601, Bio-Rad)
637 was used for the qPCR. All genes were amplified twice, and each sample was analyzed in
638 triplicate using 2X SYBR Green PCR mix (Cat#: B21202, Bimake.com) (Supplementary Table 6).
639 After normalization to *Gapdh*, the CT value was utilized to compute the fold change in RNA
640 abundance. qPCR reactions were performed using the Aria Mx Real-Time PCR equipment
641 (Agilent).
642
643 **Flow cytometry and cytokine analysis**

644 Single-cell suspensions were prepared from mouse spleen. To assess $CD4^+$ T cell activation, we
645 stained single-cell suspensions cell surface staining in 50µL FACS buffer (1% BSA, 2 mM EDTA,
646 and 0.1% sodium azide in PBS, pH 7.4) (5-10x10^5 cells/tube) and incubated with antibodies for
647 30 minutes at 37°C. (106 cells/50 mL) with anti-CD45 PercpCy5.5 (Cat# 103132, Clone#30F11,
648 BioLegend), anti-CD4 PE (Cat#100408, Clone#GK3.5, BioLegend), anti-CD44 Alexflour700
649 (Cat#103026,IM7, BioLegend), and anti-CD62L PeCy7 (Cat#104418, Clone# MEL/4, BioLegend)
650 on ice for 30 minutes (SupplementaryTable 6). Stained cells were then washed twice with 500µL
651 of ice-cold FACS buffer to eliminate binding antibodies before being analyzed immediately using
652 a BD FACSymphony A3Flow Cytometer. Annexin V APC staining cells were incubated with
653 Annexin V APC (Cat#640920, BioLegend) for 3 minutes in the ice-cold FACS buffer and then
654 washed. Followed by Propidium Iodide (Cat#6421301, BioLegend) added right before analyzing
655 the cells by FACS. MitoSpy (Cat# 424801, BioLegend) staining was carried out in accordance
656 with the manufacturer's recommendations. Cells were resuspended in MitoSpy in 300-400 µL of
657 warm 1X PBS and incubated at 37 °C for 30 minutes. Cells were then washed twice with 1X PBS
658 before being analyzed using a BD FACSymphony A3 Flow Cytometer on stained and unstained
659 samples (BD Biosciences). For inflammatory cytokines detection, sera were collected from mice
660 blood and measured by the LEGENDplex mouse inflammation panel according to the
661 manufacturer's instructions (Cat#740446, BioLegend). Samples were read on the BD
662 FACSymphony Flow Cytometer.
663
664 ***In vitro* Treg suppression assay**
665 Tregs ($CD4^+CD25^+$) cells were isolated from the spleen of sex-matched TFAM cKO and $TFAM^{f/f}$
666 (control) mice and Tconv ($CD4^+CD25^-$) from TFAM control mice using BD FACS ARIA^{TM}Ilu at the
667 UND Flow Cytometry Core: anti-CD4 PE (Cat#100408, Clone#GK3.5, BioLegend), anti-CD25
668 (Cat#102030, clone PC61, BioLegend). Afterward, 5x10^4 Tconv ($CD4^+CD25^-$) cells from TFAM
669 control were labeled with CFSE Cell Division Tracker Kit (Cat# 423801, BioLegend) and cultured
670 with mitomycin-treated wild type splenocytes. To detect Treg suppressive effect on these labeled
671 Tconv ($CD4^+CD25^-$) cells culture, we added Tregs ($CD4^+CD25^+$) from the TFAM cKO and $TFAM^{f/f}$
672 (control) for 60 hours at 37°C with 2.5 mg/mL Dynabeads^{TM} Mouse T-Activator CD3/CD28 for T-
673 Cell Expansion and Activation bead (Cat# 1145). After 60 hours, the CD4 cell proliferation was
674 observed by FACS. Suppressive capacity was calculated based on the relative proportion of
675 proliferating Tconv cells compared with cultures lacking Tregs and is presented as percent
676 suppression, as our previously described study[69].
677

678 **Cell isolation and sequencing library construction using the 10x Genomics Chromium**
679 **platform**
680 Cells were isolated from spleens from WT and cKO mice by grinding with 70 μm cell strainers
681 (Cat#22363548, Fisher brand). ACK RBC lysis buffer (Cat#A10492-01, Gibco) was used to lyse
682 RBC. Trypan blue (Cat#25900Cl, Corning) staining confirmed cell viability. The 10X Genomics
683 Chromium system was used to create 3' single-cell gene expression libraries (v3.0) from WT and
684 cKO spleen single-cell suspensions. On an Illumina HiSeq X Ten, pair-end 150 bp sequencing
685 was used to generate high-quantity data (Illumina, San Diego, California, USA). Then, using Cell
686 Ranger software v6.0.0, the output Illumina base call files from sequencing runs were combined
687 and converted to FASTQ files using Illumina's bcl2fastq.
688
689 **Single-cell RNA-seq data alignment and sample aggregating**
690 RNA reads from the 10X Chromium platform with a sequence quality of less than 30 were filtered
691 out and then mapped to the mm10 mouse reference genome using the CellRanger software
692 (v6.0.0). Seurat (v4.0.2) was used to read the individual sample output files from CellRanger
693 Count[70]. Cells were further filtered out of the downstream analysis using the following criteria:
694 *nFeature RNA <200 & nFeature RNA >4000 & percent.mt >25*. Scrublet (v0.2.3)[71] was used to
695 detect probable doublets and then *CellCycleScoring in Seurat was used* to define the cell cycle
696 phase by using a published list of cell cycle genes[72]. *SCTransform* (v0.3.2) from Seurat was used
697 to independently normalize the gene-cell count matrices with default parameters[73]. Dimension
698 reductions, including principal component analysis (PCA), clustering, and t-distributed Stochastic
699 Neighbor Embedding (t-SNE) projections (resolution =0.7) were then performed on the
700 normalized data. By following a similar pipeline, subclusters for $CD4^+$ T cells were identified.
701
702 **Cell type annotation and differential expression analysis**
703 To determine the cell type of each cluster, the *FindAllMarkers* function in Seurat was used to find
704 the cluster's gene markers. Cell types were allocated manually after consulting the CellMarker[74]
705 and PanglaoDB[75] databases. MAST (v1.18.0)[76] was utilized to conduct differential analysis on
706 each cell type to find the genes that were differentially expressed between WT and cKO cells with
707 the adjusted p-value <0.05 and absolute log2FC >0.25. The Gene Set Enrichment Analysis
708 (GSEA) with the Kyoto Encyclopedia of Genes and Genomes (KEGG) pathway annotation was
709 done using the richR package (https://github.com/hurlab/richR), with a p-value of 0.01 used as
710 the cutoff value to identify significant KEGG pathways.
711

712 **Single-cell trajectory reconstruction for CD4$^+$ T cell**

713 The Monocle2 R package (v2.20.0, http://cole-trapnell-lab.github.io/monocle-release/) was used
714 to reconstruct cell fate choices and pseudotime trajectories. The gene-cell matrix of UMI counts
715 was sent to Monocle, which then created an object using its new Cell Data Set function (*lower*
716 *Detection Limit = 0.5, expression Family = nonbinomial.size*). We evaluated the size factors and
717 dispersion of gene expression. We next used the differentialGeneTest module to conduct
718 differential expression analysis in order to determine the ordering of genes using the parameter
719 "*fullModelFormulaStr = ~celltype*," and then maintained genes with q values less than 1E-3 for
720 downstream analysis. Following the *setOrderingFilter* function, the *reduceDimension* module with
721 the argument "*method = DDRTree*" was used to reduce the dimensionality of the data. When
722 *orderCells* is executed, the root state variable may be adjusted to reflect the known biological
723 background. Following that, the *plot_cell_trajectory* and *plot_pseudotime_heatmap* functions
724 were used to visualize the data further.

725

726 **RNA velocity analysis**

727 Velocyto (v0.17.17) was used to analyze the velocity of RNA in cells[77]. This method utilizes the
728 relative amount of unspliced and spliced mRNA as a predictor of future cell state. Annotation of
729 spliced and unspliced reads was conducted using the Python script velocyto.py in the Cell Ranger
730 output folder utilizing the Velocyto pipeline. Then, the scvelo (v0.2.3)[78] was used to determine the
731 CD4$^+$ T cell velocity. The previously normalized data served as the basis for calculating first and
732 then order moments for each cell in relation to its closest neighbors (*scvelo.pp.moments(n pcs =*
733 *30, n neighbors = 30)*). Following that, the velocities were calculated, and the velocity graph was
734 produced using the *scvelo.tl.velocity* and *scvelo.tl.velocity* graph functions with the mode set to
735 'stochastic'. Finally, using the *scvelo.tl.velocity* embedding function, the velocity field was
736 projected onto the existing t-SNE coordinates.

737

738 **Transcription factor regulons prediction**

739 Gene regulatory network (GRN) was generated using pySCENIC package (v0.11.0)[79]. Briefly, the
740 raw expression matrix for the cells of all samples was filtered by keeping genes with a total
741 expression greater than 3*0.01*(number of cells). Then the *pyscenic.grn* command was used with
742 *GRNboost2* method and default options and a fixed seed to derive co-expression modules
743 between transcription factors and potential targets. The following database: cisTarget databases
744 (*mm10__refseq-r80__10kb_up_and_down_tss.mc9nr.feather, mm10__refseq-*
745 *r80__500bp_up_and_100bp_down_tss.mc9nr.feather*), the transcription factor motif annotation

746 database (*motifs-v9-nr.mgi-m0.001-o0.0.tbl*) and the list of mouse transcription factors
747 (*mm_mgi_tfs.txt*) were downloaded for the analysis. A regulon is a group of target genes regulated
748 by a common transcription factor. AUCell (Area Under the Curve) scores (regulon activities) in
749 each cell were computed with *pycenic.aucell* command (default parameters). These scores were
750 then binarized into either "on" or "off" states, by setting an optimized threshold on the distribution
751 of each regulon among all cells using the *skimage.filters.threshold_minimum* function.
752
753 **Bulk RNA-seq data processing**
754 Low quality (Q<30) reads, and sequencing adapters were removed with Trimmomatic software
755 v0.36[80] from raw reads. Clean reads were then mapped to the mouse reference genome (mm10)
756 by using HISAT2[81]. FeatureCounts[82] were used to summarize the unique mapped reads to mouse
757 genes. Differential gene expression analysis was performed using DESeq2[83] with adjusted p-
758 value <0.05 and fold change >2 as the cutoff for identifying differentially expressed genes (DEGs).
759 Gene Set Enrichment Analysis (GSEA) on KEGG pathway data was performed by using the richR
760 package and the adjusted p-value <0.05 was chosen as the cutoff value to select significant
761 KEGG pathways.
762
763 **Microbiome analysis**
764 Microbial DNA samples were collected as our vius published protocol[33]. Samples were sequenced
765 using Oxford Nanopore Technology. Raw sequencing data underwent quality control using
766 Porechop (v1.0.0) to remove adapter sequences, followed by length filtering with NanoFilt to
767 retain sequences between 1,200 and 1,800 base pairs. Quality metrics were assessed using
768 NanoStat. Chimeric reads were identified and removed through an all-versus-all alignment
769 approach using minimap2 (v2.17) with Oxford Nanopore-specific parameters (-x ava-ont -g 500),
770 followed by filtering with yacrd (coverage threshold 4, noise threshold 0.4). Cleaned reads were
771 mapped against a reference database using minimap2 (-x map-ont), and high-confidence
772 alignments were retained using custom filtering scripts from the Spaghetti pipeline. OTU tables
773 and taxonomy assignments were generated for downstream analysis.
774
775 Microbiome analysis was performed in R (version ≥4.0.0) using the phyloseq package. Alpha
776 diversity (Observed richness, Simpson, and Shannon indices) was calculated at the genus level.
777 Beta diversity was assessed using Bray-Curtis dissimilarity and visualized with Principal
778 Coordinates Analysis (PCoA). Differential abundance analysis between experimental groups
779 (P8M, P8W, PT, and PY) was conducted using ALDEx2 with 128 Monte Carlo instances. To

780 identify significantly differentially abundant bacterial taxa between groups, we used the ALDEx2
781 package[84] . This approach was chosen to properly handle the compositional nature of microbiome
782 data. Four comparisons were performed: P8M vs P8W, PT vs PY, P8W vs PY, and PT vs P8M.
783 For each comparison, Monte Carlo sampling with 128 Dirichlet instances was used to account for
784 technical variation (mc.samples = 128), with all features included in the geometric mean
785 calculation (denom = "all").Bacterial taxa were considered significantly differentially abundant if
786 they met both thresholds: p-value < 0.05 (Welch's t-test) and effect size > 0.8. The effect size
787 threshold represents cases where the between-group difference exceeds 80% of the maximum
788 within-group dispersion[85] . Pathway functionality was predicted from the taxonomic data using
789 PICRUSt2 (Phylogenetic Investigation of Communities by Reconstruction of Unobserved States),
790 allowing for inference of KEGG pathways present in the microbial communities based on marker
791 gene sequencing data. Significant pathways (p <0.05) were visualized using heatmaps.
792
793 **Antibiotic Treatment and Fecal Microbiota Transplantation (FMT)**
794 To deplete endogenous microbiota, mice were administered a broad-spectrum antibiotic cocktail
795 in drinking water for two weeks: ampicillin (10 mg/mL, A1593, MilliporeSigma), metronidazole (10
796 mg/mL, PHR1052, MilliporeSigma), and vancomycin hydrochloride (5 mg/mL, SBR00001,
797 MilliporeSigma). Fecal material for transplantation was collected from donor mice aged 8 weeks
798 (young) or 2 years (aged), snap-frozen, and stored at -80°C. Following antibiotic treatment,
799 recipient C57BL/6 mice were housed in sterile, autoclaved cages and orally gavaged with 300–
800 400 µL of freshly prepared fecal suspension from untreated donor mice. The suspension was
801 generated by homogenizing fecal pellets in sterile water. Control groups received either sterile
802 water or autologous fecal homogenates.
803
804 **Grip strength analysis**
805 Neuromuscular strength was assessed using the grip strength test. The forelimb and hindlimb
806 grip strengths of mice were assessed by using a grip strength meter from San Diego Instruments.
807 Each mouse was tested in three trials, and the force was recorded as grams-force (gf, 1 gf = 9.8
808 x 10^{-3} Newtons).
809
810 **Open field test**
811 Locomotor activity was measured in the open field test. A mouse was placed in the empty square
812 cage from San Diego Instruments. Total distance (m) covered during a 10-min period was
813 recorded and calculated by ANY-maze software (version 7.1).

814 **Data availability**

815 Datasets generated in this study by RNA-seq and scRNA-seq are accessible at GSE203143
816 (Reviewer access token: ozebasggjbyrpsf) and GSE197973 (Reviewer access token:
817 clajaakoztkhtyh), respectively. All data associated with this study are present in the paper or the
818 Supplementary Materials.

819

820 **Code availability**

821 All data analysis scripts are available on the GitHub (https://github.com/guokai8/TFAM).

822

823 **Figure Legends**

824 **Figure 1. Treg-intrinsic TFAM loss reprograms CD4$^+$ T cell lineage fate toward pro-**
825 **inflammatory and terminal effector states.**

826 (**A**) Schematic representation of the experimental workflow. Splenocytes were isolated from
827 Foxp3^{Cre}Tfam$^{f/f}$ (TFAM cKO) and Tfam$^{f/f}$ (WT) mice for single-cell RNA sequencing (scRNA-seq)
828 and downstream analysis.

829 (**B**) UMAP projection of 49,156 immune cells (WT: 34,958; cKO: 14,198), identifying 21 major
830 immune subsets across 26 transcriptional clusters. Erythroid lineage cells were excluded.

831 (**C**) UMAP projection of CD4$^+$ T cells (WT: 4,324; cKO: 3,497), revealing six transcriptionally
832 distinct subsets: naïve, effector memory (TEM), exhausted, natural Tregs (nTregs),
833 aged/dysfunctional Tregs (aTregs), and cytotoxic CD4$^+$ T cells.

834 (**D**) Track plot showing representative gene expression patterns across single CD4$^+$ T cells. Rows
835 represent genes; columns represent individual cells.

836 (**E**) Bar graph quantifying relative abundance of CD4$^+$ T cell subsets in WT and cKO mice. TFAM
837 deficiency promotes expansion of effector-like states (aTregs, cytotoxic, and TEM), with reduced
838 naïve and exhausted populations.

839 (**F**) Gene set enrichment analysis (GSEA) of KEGG pathways shows increased TNFα signaling,
840 cytokine/chemokine responses, and calcium flux in CD4$^+$ T cells from TFAM cKO mice.

841 (**G**) Pseudotime trajectory analysis (Monocle) of CD4$^+$ T cells reveal two dominant differentiation
842 paths (P1 and P2). TFAM-deficient cells preferentially adopt the alternative P2 trajectory, enriched
843 in transcriptional States 1 and 2.

844 (**H**) Monocle 2 trajectory cell states for all CD4$^+$ T cells, each branch represents one cell state
845 (left). Barplots representing cell proportions in the seven states of WT and cKO (right). Cells are
846 colored according to seven states, which partition the trajectory.

847 (**I**)**.** Relative proportion of $CD4^+$ T cells among different states of WT and cKO spleen, color stands
848 for cell type.
849 (**J**) RNA velocity analysis confirms directionality of lineage bifurcation, with streamlines overlaid
850 on UMAP embedding indicating transcriptional flow.
851 (**K**) Heatmap of four gene clusters ordered by pseudotime. Cluster 1 genes (e.g., Klf3, Bcl2) mark
852 early developmental states; Cluster 2 genes (e.g., Ccl5, S100a6) are linked to terminal effector
853 function and inflammation. KEGG pathway enrichment of cluster-specific genes is shown.
854 (**L**) Representative flow cytometry plots of $CD4^+CD44^{hi}CD62L^{lo}$ effector and $CD4^+CD44^{lo}CD62L^{hi}$
855 naïve T cells in spleen and lymph nodes from WT and TFAM cKO mice.
856 (**M**) Quantification of mean fluorescence intensity (MFI) for effector and naïve $CD4^+$ T cells across
857 organs. TFAM cKO mice exhibit increased effector T cell signatures.
858 (**N**) Suppression assay showing reduced regulatory function of TFAM-deficient Tregs in vitro. Co-
859 culture with CFSE-labeled $CD4^+$ Tconv cells demonstrates impaired suppression of proliferation
860 upon CD3/CD28 stimulation.
861
862 **Figure 2. Treg-intrinsic TFAM loss triggers a multi-lineage stress response, inflammatory**
863 **reprogramming, and systemic senescence.**
864 (**A**) Gene regulatory network (GRN) inference from scRNA-seq data identified 177 regulons
865 across $CD4^+$ T cell subsets. TFAM cKO Tregs showed increased inflammatory activity (Nfkb2,
866 Nfatc1, Rora, Runx2), stress-responsive (Egr1, Junb, Xbp1), and cytotoxic (Runx3) regulons,
867 alongside pan-$CD4^+$ expression of the mitochondrial stress gene Ddit3.
868 (**B**) Dot plots showing upregulation of key inflammatory transcriptional regulators (Prdm1, Nfkb1,
869 Nfkb2, Ahr) in TFAM-deficient Tregs.
870 (**C**) Gene set enrichment analysis (GSEA) shows significant pathways in Monocytes (Mono),
871 Macrophages (Mac), dendritic cell (DC), Immature Dendritic Cells (iDC) and Plasmacytoid
872 Dendritic Cells (pDC) cells in TFAM cKO mice.
873 (**D**) Bulk RNA-seq of cKO spleens revealed enrichment of cell death pathways, including
874 apoptosis and necroptosis.
875 (**E**) Immunoblots confirmed caspase-3 and -8 cleavage, IκBα degradation, and phosphorylation
876 of RIPK1, RIPK3, and MLKL, indicative of RIPK-mediated immunogenic cell death.
877 (**F**) Histological analysis revealed multi-organ inflammatory infiltration in colon, liver, lung, and
878 kidney of TFAM cKO mice.
879 (**G**) H&E staining of femurs showed pronounced cortical bone thinning in TFAM cKO animals.

880 (**H**) Spleens from TFAM cKO mice exhibited splenomegaly, follicular disruption, and marginal
881 zone disorganization.
882 (**I**) Mitospy staining in sorted Tregs revealed mitochondrial depolarization and elevated oxidative
883 stress in TFAM-deficient cells.
884 (**J**) Elevated circulating levels of TNF-α, IL-6, and IFNγ in serum from TFAM cKO mice, confirming
885 systemic inflammation.
886 (**K**) RT-qPCR showed increased expression of Cdkn2a (p16) and Cdkn1a (p21);
887 (**L**) Immunoblotting of splenic lysates confirmed elevated levels of p53, CDK4, PCNA, p16, and
888 p21, consistent with senescence-associated gene expression.
889 (**M**) Whole-spleen RNA-seq revealed enrichment of aging- and inflammation-associated gene
890 networks.
891 (**N**) GSEA showed significant upregulation of pathways linked to neuroactive ligand–receptor
892 signaling, and downregulation of circadian rhythm disruption, and protein trafficking which are
893 hallmarks of systemic immune aging.
894
895 **Figure 3. Partial TFAM reduction in Tregs promotes systemic aging features, peripheral**
896 **inflammation, and early neurodegenerative changes.**
897 (**A**) Human PBMC transcriptome analysis reveals age-associated decline in TFAM expression,
898 supporting its role as a mitochondrial-immune rheostat.
899 (**B-C**) TFAM Het (Foxp3^{Cre}Tfam$^{f/+}$) mice develop aging phenotypes, including kyphosis and
900 reduced body weight, by 8-10 months of age.
901 (**D**) Circulating TNF-α and IL-6 levels are elevated in TFAM Het mice, indicating persistent low-
902 grade systemic inflammation.
903 (**E**) Splenic CD4^{+} T cells isolated from TFAM Het mice display elevated expression of
904 senescence-associated markers, including Cdkn2a (*p16^Ink4a*), Cdkn1a (*p21^Cip1*), p53, and
905 CDK4, with GAPDH serving as the loading control.
906 (**F**) Neuromuscular assessment shows reduced forelimb grip strength in TFAM Het mice.
907 (**G**) Open field behavioral assay demonstrates decreased exploratory behavior and locomotor
908 hypoactivity, consistent with CNS dysfunction.
909 (**H–I**) Cresyl violet staining reveals neuronal loss in the hippocampus and cortex of 8-month-old
910 TFAM Het mice compared to 8-week controls.
911 (**J**) Longitudinal hippocampal RNA-seq profiling shows minimal transcriptional changes at 8
912 weeks but extensive neuroimmune remodeling by 8 months.

913 (**K**) Heatmap displaying upregulation of neuroinflammation-associated genes (Gabra5, Slc38a5,
914 Calcr, Ganbare) in 8-month TFAM Het hippocampus.
915 (**L**) KEGG pathway enrichment of 8-month hippocampal transcriptomes identify significant
916 enriched pathways of oxidative stress, inflammatory signaling, and neurodegeneration-linked
917 pathways.
918
919 **Figure 4. TFAM insufficiency in Tregs triggers CNS immune activation and microglial**
920 **sensitization to TNF signaling.**
921 (**A-B**) Iba1 and NeuN immunohistochemistry shows widespread activation of amoeboid microglia
922 in the cortex and hippocampus of 8-month-old TFAM Het mice, with concurrent neuronal loss.
923 (**C**) Flow cytometric analysis reveals increased MHC-I expression on brain-resident $CX3CR1^+$
924 microglia from TFAM Het mice, consistent with enhanced antigen presentation.
925 (**D**) Ex vivo stimulation with TNF-α induces elevated *Il1b*, *Tnfr1*, and *Il6* expression in $CX3CR1^+$
926 microglia from TFAM Het brains, indicating heightened inflammatory sensitivity.
927
928 **Figure 5. TFAM insufficiency in Tregs drives microbiota–lipid dysregulation and**
929 **neuroinflammatory reprogramming via the gut–brain–immune axis.**
930 (**A**) Longitudinal 16S rRNA sequencing reveals significantly elevated α-diversity (Shannon and
931 Simpson indices) in TFAM Het mice, peaking at 8 months of age.
932 (**B**) β-diversity analysis (Bray–Curtis dissimilarity) demonstrates genotype- and age-specific
933 microbial clustering, indicating progressive community remodeling.
934 (**C**) Phylum-level taxonomic profiling reveals expansion of *Campilobacterota* and depletion of
935 *Bacteroidota* in aged TFAM Het mice, signatures linked to inflammaging.
936 (**D**) VennDiagram depicting distribution and overlap of microbial species across genotypes and
937 age groups.
938 (**E**) Differential abundance analysis identifies 18 significantly altered taxa, including loss of key
939 SCFA-producing genera (*Lactobacillus murinus*, *Odoribacter*, *Prevotellaceae_UCG-001*) in
940 TFAM Het mice.
941 (**F**) KEGG-based predictive metagenomics shows TFAM Het microbiota enriched in age-related
942 pathways including FoxO, and spinocerebellar ataxia signaling.
943 (**G**) Lipid metabolism pathways, including unsaturated fatty acid biosynthesis, bile acid
944 biosynthesis, and sphingolipid metabolism, are significantly altered. Neurotransmission pathways
945 (GABAergic, glutamatergic synapses) are also enriched in aged TFAM Het mice.

946 (**H**) Microbiota–host gene co-correlation network analysis reveals 323 significant interactions.
947 Notably, *Helicobacter* positively correlates with *Ntsr2*, while Lactobacillus inversely correlates with
948 neuroendocrine (e.g., *Pomc*, *Sstr5*) and developmental genes (*Elk3*, *Sox4*) and positively
949 correlates with inflammatory genes (*Mpo*, *Ifitm6*). *Lachnospiraceae_NK4A136_group* links to
950 complement-mediated inflammation (*C5ar2*).
951 (**I**) RT-qPCR validation confirms elevated expression of *Il1b* and *Tnfr1* in peripheral tissues from
952 TFAM Het mice, supporting a chronic inflammatory state.
953
954 **Figure 6. Restoration of mitochondrial fitness mitigates inflammation and functional**
955 **decline in models of immune aging.**
956 (**A**) Schematic of therapeutic intervention in TFAM cKO mice. Mice received intraperitoneal
957 resveratrol (RSV; 7 mg/kg) every other day for 4 weeks.
958 (**B**) Mitospy staining in skin tissue reveals enhanced mitochondrial membrane potential in RSV-
959 treated TFAM cKO mice, indicating improved mitochondrial integrity.
960 (**C**) Serum levels of TNF-α and IL-6 were significantly reduced following RSV treatment, reflecting
961 dampened systemic inflammation.
962 (**D-F**) Quantitative RT-PCR analysis of splenocytes shows reduced expression of senescence
963 markers Cdkn2a ($p16^{Ink4a}$) and Cdkn1a ($p21^{Cip1}$) in RSV-treated mice, consistent with suppression
964 of the senescence-associated secretory phenotype (SASP).
965 (**G**) Histological examination of lung, liver, and kidney shows decreased inflammatory infiltration
966 and preserved tissue structure in RSV-treated animals.
967 (**H**) Experimental design for fecal microbiota transplantation (FMT) in TFAM Het mice. Mice were
968 antibiotic-conditioned for 10 days and subsequently gavage feces from TFAM-sufficient donors
969 over 3 days, followed by a 3-week recovery.
970 (**I**) FMT improved neuromuscular performance, demonstrated by increased rotarod endurance
971 and forelimb grip strength. These improvements were associated with re-expression of Treg-
972 associated genes and suppression of pro-inflammatory programs.
973 (**J**) Working model summarizing the role of TFAM as a central regulator of mitochondrial redox
974 balance, microbiota composition, and immune aging. Restoration of mitochondrial integrity via
975 RSV and microbial reprogramming via FMT ameliorates immunopathology and rejuvenates
976 immune function.
977
978 **Supplementary Fig. 1: Landscape of scRNA-seq analysis of WT and cKO spleen.**

979 **A.** t-SNE projections of single-cell transcriptomes from WT and cKO mice before Erythroid cells
980 were removed, annotated by cell type. Each dot denotes a distinct cell. **B.** Cell subset proportions
981 (top) and numbers (bottom) for WT and cKO spleens. **C.** Dot plot of mean expression of canonical
982 marker genes for 20 major lineages from tissues of each origin, as indicated. **D.** Gene Set
983 Enrichment Analysis (GSEA) of KEGG pathways for all cell types between cKO and WT (Only
984 age-related pathways are selected). Color stands for the up-regulated (red) or down-regulated
985 (blue) in cKO spleen. Enriched terms were identified as significant at a p-value ≤ 0.01. **E.**
986 Expression of aged-related genes (*Fcer2a*, *Cd79b*, *Zfp36l2*, and *S100a6*) on Figure 1B t-SNE
987 embedding. Each dot corresponds to a single cell.
988
989 **Supplementary Fig. 2: scRNA-seq results show the cellular heterogeneity in CD4$^+$ T cells.**
990 **A.** Relative proportion of CD4$^+$ T cells among WT and cKO spleen, color stands for cell type. **B.**
991 Violin plot showing the expression profile of age-related genes among all CD4$^+$ T cells. **C.** Monocle
992 2 prediction of CD4$^+$ T cell subsets developmental trajectory with pseudotime. Each dot
993 represents an individual cell. **D.** Functional enrichment analysis of KEGG pathways with up-
994 regulated differential expressed genes for the cell states. Only the top 20 of the enriched pathways
995 were plotted from each state.
996
997 **Fig. 3: t-SNE projection of binary regulon activity.** t-SNE plots visualize the binarized regulon
998 activity states of Irf8, Runx2, Bcl11a, and Nfkb1 across single cells, highlighting distinct
999 transcriptional regulatory modules and cell-type-specific activation patterns.
1000
1001 **Supplementary Fig. 4: TFAM deletion in Foxp3$^+$ Tregs induces systemic pathology and**
1002 **accelerates immune aging in Foxp3^{Cre}Tfam$^{f/f}$ mice. A.** Representative photograph showing the
1003 deteriorated physical appearance of a cKO mouse (right) compared to an age- and sex-matched
1004 WT littermate (left) at 8 weeks of age. **B.** X-ray image depicting increased spinal curvature in the
1005 cKO mouse (right) relative to a WT littermate (left) of the same age and sex. **C.** Kaplan-Meier
1006 survival analysis comparing WT (n=10; M/F) and cKO (n=10; M/F) mice, revealing reduced
1007 lifespan in cKO animals. **E.** Flow cytometric analysis of Annexin V staining in spleen and skin cells
1008 from WT and cKO mice, indicating increased cell death in cKO tissues. **F**. Mitospy staining of
1009 splenocytes from WT and cKO mice, assessed by flow cytometry and presented as a
1010 fluorescence intensity histogram, showing mitochondrial alterations in cKO cells.
1011

1012 **Supplementary Fig. 5: Increased cell infiltration and inflammation in different organs in**
1013 **Foxp3^{Cre}Tfam$^{f/f}$ mice. A.** Histology sections stained with H&E from lung, liver, colon, and kidney.
1014 **B.** Serum cytokines identified by Legend plex for IL-1β, IL-10, MCP1, IL-23, IL-1α, IL-17, IFNγ,
1015 IL-12, IFNβ, GM-CSF, and IL-27 with estimated values displayed. Data represented as mean ±
1016 SD. Statistical test used: t-test, WT (n=5-10; M/F) and cKO mice (n=5-10, M/F).
1017
1018 **Supplementary Fig. 6: Restoration of mitochondrial function leads to mitigate pathologies.**
1019 **A-B.** Body weight (**C**) and fold change (**D**) of young and old WT and cKO mice. Data represented
1020 as mean ± SD. Statistical test used: two-way ANOVA with post-hoc test (C). WT (n=5; M/F) and
1021 Het mice (n=5, M/F).
1022
1023 **Supplementary Table 1:** Gene Set Enrichment Analysis (GSEA) of KEGG pathway between
1024 cKO and WT for all cell types.
1025
1026 **Supplementary Table 2:** Gene Set Enrichment Analysis (GSEA) of KEGG pathway between
1027 cKO and WT for CD4 subsets.
1028 **Supplementary Table 3:** Functional enrichment analysis of KEGG pathway for four clusters.
1029
1030 **Supplementary Table 4:** Functional enrichment analysis of KEGG pathway for Monocle states.
1031
1032 **Supplementary Table 5:** Gene Set Enrichment Analysis (GSEA) of KEGG pathway between
1033 cKO and WT from Brain, Spleen and Skin RNA-seq.
1034
1035 **Supplementary Table 6:** Primer sequences for RT-qPCR, antibodies for Western blots and flow
1036 cytometry, and other reagents.
1037
1038 **Acknowledgments**
1039 We thank Kristian Herman, Reet Goyal, Risha Mathur, Leia Laurer, Sofie Robinson, and Harpreet
1040 Singh for assistance with cell culture, mouse experiments, and general laboratory support.
1041 Technical support was provided by Dr. Bony De Kumar and Damien Parrello (Genomics Core),
1042 Steve Anderson and Subha Nookala (Flow Cytometry Core), Neeta Adhikari and Donna Laturnus
1043 (Histology Core), Sarah Abrahamson (Imaging Core), Ellen Olson and Dr. Collin Combs (Behavior
1044 Core), and Dr. Brett McGregor (Computational Data Analysis Core) at the University of North
1045 Dakota.

Fundings

Research reported in this publication was supported by NIH Host–Pathogen Interactions COBRE Pilot Grant (NIGMS/NIH P20GM1034442 to X.W. and R.M.) and the DaCCOTA Pilot Grant (NIGMS/NIH U54GM128729 to R.M. and D.A.J.). TRANCENDS Pilot Grant NIGMS/NIH P20GM155890 to RM. E.A. and J.G. were supported by the Eva Gilbertson, M.D. Foundation Study Grant to J.D. Core facilities were supported by NIH/NIGMS awards P20GM113123 and U54GM128729. The graphical abstract was created using Servier Medical Art (https://smart.servier.com) under a Creative Commons Attribution 3.0 License.

Contributions

R.M. conceived and designed the study. K.G., R.M., J.G., and Z.W. analyzed and interpreted the scRNA-seq and RNA-seq data. T.D., Z.W., J.G., B.B., H.M., A.L., R.P., M.R., and S.J. performed the experiments. R.M., K.G., J.G., and Z.W. prepared the figures and wrote the manuscript. R.M., J. G., H.C., K.G., N.K., J.H., Z.W., D.J., H.B., M.G., and A.T. critically reviewed and revised the manuscript. All authors contributed to discussions and approved the final version.

Competing interests

The authors declare no competing interests.

1064 **References**
1065

1066 1. Goronzy, J.J. & Weyand, C.M. Mechanisms underlying T cell ageing. *Nat Rev Immunol*
1067 **19**, 573-583 (2019).

1068
1069 2. Nikolich-Zugich, J. The twilight of immunity: emerging concepts in aging of the immune
1070 system. *Nat Immunol* **19**, 10-19 (2018).

1071
1072 3. Shaw, A.C., Goldstein, D.R. & Montgomery, R.R. Age-dependent dysregulation of innate
1073 immunity. *Nat Rev Immunol* **13**, 875-887 (2013).

1074
1075 4. Franceschi, C. *et al.* Inflamm-aging. An evolutionary perspective on immunosenescence.
1076 *Ann N Y Acad Sci* **908**, 244-254 (2000).

1077
1078 5. Li, X., Liang, Y., LeBlanc, M., Benner, C. & Zheng, Y. Function of a Foxp3 cis-element
1079 in protecting regulatory T cell identity. *Cell* **158**, 734-748 (2014).

1080
1081 6. Olusanya, B.O. Surrogate measurements for identifying newborns with low birth weight
1082 in a community with predominant non-hospital births. *J Child Health Care* **14**, 386-395
1083 (2010).

1084
1085 7. Josefowicz, S.Z., Lu, L.F. & Rudensky, A.Y. Regulatory T cells: mechanisms of
1086 differentiation and function. *Annu Rev Immunol* **30**, 531-564 (2012).

1087
1088 8. Sakaguchi, S. *et al.* Regulatory T Cells and Human Disease. *Annu Rev Immunol* **38**, 541-
1089 566 (2020).

1090
1091 9. Angelin, A. *et al.* Foxp3 Reprograms T Cell Metabolism to Function in Low-Glucose,
1092 High-Lactate Environments. *Cell Metab* **25**, 1282-1293 e1287 (2017).

1093
1094 10. Cascone, T. *et al.* Increased Tumor Glycolysis Characterizes Immune Resistance to
1095 Adoptive T Cell Therapy. *Cell Metab* **27**, 977-987 e974 (2018).

1096
1097 11. Klarquist, J. *et al.* Clonal expansion of vaccine-elicited T cells is independent of aerobic
1098 glycolysis. *Sci Immunol* **3** (2018).

1099
1100 12. Fu, Z. *et al.* Requirement of Mitochondrial Transcription Factor A in Tissue-Resident
1101 Regulatory T Cell Maintenance and Function. *Cell Rep* **28**, 159-171 e154 (2019).

1102

1103 13. Zheng, Y. *et al.* Role of conserved non-coding DNA elements in the Foxp3 gene in
1104 regulatory T-cell fate. *Nature* **463**, 808-812 (2010).

1105
1106 14. Grinberg-Bleyer, Y. *et al.* NF-kappaB c-Rel Is Crucial for the Regulatory T Cell Immune
1107 Checkpoint in Cancer. *Cell* **170**, 1096-1108 e1013 (2017).

1108
1109 15. Oh, H. *et al.* An NF-kappaB Transcription-Factor-Dependent Lineage-Specific
1110 Transcriptional Program Promotes Regulatory T Cell Identity and Function. *Immunity* **47**,
1111 450-465 e455 (2017).

1112
1113 16. Chapman, N.M. *et al.* mTOR coordinates transcriptional programs and mitochondrial
1114 metabolism of activated T(reg) subsets to protect tissue homeostasis. *Nat Commun* **9**, 2095
1115 (2018).

1116
1117 17. Desdin-Mico, G. *et al.* T cells with dysfunctional mitochondria induce multimorbidity and
1118 premature senescence. *Science* **368**, 1371-1376 (2020).

1119
1120 18. Gill, J.S. *et al.* Mitochondrial Oxidative Stress Regulates FOXP3+ T-Cell Activity and
1121 CD4-Mediated Inflammation in Older Adults with Frailty. *Int J Mol Sci* **25** (2024).

1122
1123 19. Lahl, K. & Sparwasser, T. In vivo depletion of FoxP3+ Tregs using the DEREG mouse
1124 model. *Methods Mol Biol* **707**, 157-172 (2011).

1125
1126 20. Hanakawa, S., Chow, Z. & Kabashima, K. Depletion of Treg by the Diphtheria Toxin
1127 System. *Methods Mol Biol* **2559**, 31-39 (2023).

1128
1129 21. Brunkow, M.E. *et al.* Disruption of a new forkhead/winged-helix protein, scurfin, results
1130 in the fatal lymphoproliferative disorder of the scurfy mouse. *Nat Genet* **27**, 68-73 (2001).

1131
1132 22. Weinberg, S.E. *et al.* Mitochondrial complex III is essential for suppressive function of
1133 regulatory T cells. *Nature* **565**, 495-499 (2019).

1134
1135 23. Soto-Heredero, G., Desdin-Mico, G. & Mittelbrunn, M. Mitochondrial dysfunction defines
1136 T cell exhaustion. *Cell Metab* **33**, 470-472 (2021).

1137
1138 24. Larsson, N.G. *et al.* Mitochondrial transcription factor A is necessary for mtDNA
1139 maintenance and embryogenesis in mice. *Nat Genet* **18**, 231-236 (1998).

1140
1141 25. West, A.P. & Shadel, G.S. Mitochondrial DNA in innate immune responses and
1142 inflammatory pathology. *Nat Rev Immunol* **17**, 363-375 (2017).

1143
1144 26. Kuroda, R. *et al.* Loss of mitochondrial transcription factor A in neural stem cells leads to
1145 immature brain development and triggers the activation of the integral stress response in
1146 vivo. *PLoS One* **16**, e0255355 (2021).

1147
1148 27. Lu, T. *et al.* TFAM deficiency in dendritic cells leads to mitochondrial dysfunction and
1149 enhanced antitumor immunity through cGAS-STING pathway. *J Immunother Cancer* **11**
1150 (2023).

1151
1152 28. West, A.P. *et al.* Mitochondrial DNA stress primes the antiviral innate immune response.
1153 *Nature* **520**, 553-557 (2015).

1154
1155 29. Elyahu, Y. *et al.* Aging promotes reorganization of the CD4 T cell landscape toward
1156 extreme regulatory and effector phenotypes. *Sci Adv* **5**, eaaw8330 (2019).

1157
1158 30. Furman, D. *et al.* Chronic inflammation in the etiology of disease across the life span. *Nat*
1159 *Med* **25**, 1822-1832 (2019).

1160
1161 31. Garg, S.K. *et al.* Aging is associated with increased regulatory T-cell function. *Aging Cell*
1162 **13**, 441-448 (2014).

1163
1164 32. Amorim, J.A. *et al.* Mitochondrial and metabolic dysfunction in ageing and age-related
1165 diseases. *Nat Rev Endocrinol* **18**, 243-258 (2022).

1166
1167 33. Wang, Z. *et al.* Age-related dysregulation of intestinal epithelium fucosylation is linked to
1168 an increased risk of colon cancer. *JCI Insight* **9** (2024).

1169
1170 34. Gomez de Las Heras, M.M. *et al.* CD4 T cell therapy counteracts inflammaging and
1171 senescence by preserving gut barrier integrity. *Sci Immunol* **10**, eadv0985 (2025).

1172
1173 35. Claesson, M.J. *et al.* Gut microbiota composition correlates with diet and health in the
1174 elderly. *Nature* **488**, 178-184 (2012).

1175
1176 36. Smith, P.M. *et al.* The microbial metabolites, short-chain fatty acids, regulate colonic Treg
1177 cell homeostasis. *Science* **341**, 569-573 (2013).

1178
1179 37. Thevaranjan, N. *et al.* Age-Associated Microbial Dysbiosis Promotes Intestinal
1180 Permeability, Systemic Inflammation, and Macrophage Dysfunction. *Cell Host Microbe*
1181 **21**, 455-466 e454 (2017).

1182

1183 38. Sanna, S. *et al.* Causal relationships among the gut microbiome, short-chain fatty acids and
1184 metabolic diseases. *Nat Genet* **51**, 600-605 (2019).

1185
1186 39. Zhou, D. *et al.* Sodium butyrate attenuates high-fat diet-induced steatohepatitis in mice by
1187 improving gut microbiota and gastrointestinal barrier. *World J Gastroenterol* **23**, 60-75
1188 (2017).

1189
1190 40. Stilling, R.M. *et al.* The neuropharmacology of butyrate: The bread and butter of the
1191 microbiota-gut-brain axis? *Neurochem Int* **99**, 110-132 (2016).

1192
1193 41. Furusawa, Y. *et al.* Commensal microbe-derived butyrate induces the differentiation of
1194 colonic regulatory T cells. *Nature* **504**, 446-450 (2013).

1195
1196 42. Louis, P. & Flint, H.J. Formation of propionate and butyrate by the human colonic
1197 microbiota. *Environ Microbiol* **19**, 29-41 (2017).

1198
1199 43. Arpaia, N. *et al.* Metabolites produced by commensal bacteria promote peripheral
1200 regulatory T-cell generation. *Nature* **504**, 451-455 (2013).

1201
1202 44. Fang, P., Kazmi, S.A., Jameson, K.G. & Hsiao, E.Y. The Microbiome as a Modifier of
1203 Neurodegenerative Disease Risk. *Cell Host Microbe* **28**, 201-222 (2020).

1204
1205 45. Wilmanski, T. *et al.* Gut microbiome pattern reflects healthy ageing and predicts survival
1206 in humans. *Nat Metab* **3**, 274-286 (2021).

1207
1208 46. Valdes, A.M., Walter, J., Segal, E. & Spector, T.D. Role of the gut microbiota in nutrition
1209 and health. *BMJ* **361**, k2179 (2018).

1210
1211 47. Johnson, E.L., Heaver, S.L., Walters, W.A. & Ley, R.E. Microbiome and metabolic
1212 disease: revisiting the bacterial phylum Bacteroidetes. *J Mol Med (Berl)* **95**, 1-8 (2017).

1213
1214 48. Wu, S.K., Wang, L., Wang, F. & Zhang, J. Resveratrol improved mitochondrial biogenesis
1215 by activating SIRT1/PGC-1alpha signal pathway in SAP. *Sci Rep* **14**, 26216 (2024).

1216
1217 49. Price, N.L. *et al.* SIRT1 is required for AMPK activation and the beneficial effects of
1218 resveratrol on mitochondrial function. *Cell Metab* **15**, 675-690 (2012).

1219
1220 50. Franceschi, C., Garagnani, P., Parini, P., Giuliani, C. & Santoro, A. Inflammaging: a new
1221 immune-metabolic viewpoint for age-related diseases. *Nat Rev Endocrinol* **14**, 576-590
1222 (2018).

1223
1224 51. Campisi, J. *et al.* From discoveries in ageing research to therapeutics for healthy ageing.
1225 *Nature* **571**, 183-192 (2019).

1226
1227 52. Lopez-Otin, C., Blasco, M.A., Partridge, L., Serrano, M. & Kroemer, G. The hallmarks of
1228 aging. *Cell* **153**, 1194-1217 (2013).

1229
1230 53. Shin, B. *et al.* Mitochondrial Oxidative Phosphorylation Regulates the Fate Decision
1231 between Pathogenic Th17 and Regulatory T Cells. *Cell Rep* **30**, 1898-1909 e1894 (2020).

1232
1233 54. Liu, X. *et al.* Regulation of mitochondrial biogenesis in erythropoiesis by mTORC1-
1234 mediated protein translation. *Nat Cell Biol* **19**, 626-638 (2017).

1235
1236 55. Viader, A. *et al.* Aberrant Schwann cell lipid metabolism linked to mitochondrial deficits
1237 leads to axon degeneration and neuropathy. *Neuron* **77**, 886-898 (2013).

1238
1239 56. Kim, J. *et al.* Cutting edge: depletion of Foxp3+ cells leads to induction of autoimmunity
1240 by specific ablation of regulatory T cells in genetically targeted mice. *J Immunol* **183**,
1241 7631-7634 (2009).

1242
1243 57. Baker, D.J. *et al.* BubR1 insufficiency causes early onset of aging-associated phenotypes
1244 and infertility in mice. *Nat Genet* **36**, 744-749 (2004).

1245
1246 58. Niedernhofer, L.J. *et al.* A new progeroid syndrome reveals that genotoxic stress
1247 suppresses the somatotroph axis. *Nature* **444**, 1038-1043 (2006).

1248
1249 59. Osorio, F.G. *et al.* Nuclear envelope alterations generate an aging-like epigenetic pattern
1250 in mice deficient in Zmpste24 metalloprotease. *Aging Cell* **9**, 947-957 (2010).

1251
1252 60. Vacca, M. *et al.* The Controversial Role of Human Gut Lachnospiraceae. *Microorganisms*
1253 **8** (2020).

1254
1255 61. Bettedi, L., Yan, A., Schuster, E., Alic, N. & Foukas, L.C. Increased mitochondrial and
1256 lipid metabolism is a conserved effect of Insulin/PI3K pathway downregulation in adipose
1257 tissue. *Sci Rep* **10**, 3418 (2020).

1258
1259 62. Martins, R., Lithgow, G.J. & Link, W. Long live FOXO: unraveling the role of FOXO
1260 proteins in aging and longevity. *Aging Cell* **15**, 196-207 (2016).

1261

1262 63. Chai, J.N. *et al.* Helicobacter species are potent drivers of colonic T cell responses in
1263 homeostasis and inflammation. *Sci Immunol* **2** (2017).

1264
1265 64. Lagouge, M. *et al.* Resveratrol improves mitochondrial function and protects against
1266 metabolic disease by activating SIRT1 and PGC-1alpha. *Cell* **127**, 1109-1122 (2006).

1267
1268 65. Cryan, J.F. *et al.* The Microbiota-Gut-Brain Axis. *Physiol Rev* **99**, 1877-2013 (2019).

1269
1270 66. O'Toole, P.W. & Jeffery, I.B. Gut microbiota and aging. *Science* **350**, 1214-1215 (2015).

1271
1272 67. Mathur, R. *et al.* A mouse model of Salmonella typhi infection. *Cell* **151**, 590-602 (2012).

1273
1274 68. Mathur, R., Alam, M.M., Zhao, X.-F., Huang, Y. & Zhu, X. Mechanistic insight into the
1275 development of TNBS-mediated intestinal fibrosis and evaluating the inhibitory effects of
1276 rapamycin. *JoVE (Journal of Visualized Experiments)*, e60067 (2019).

1277
1278 69. Park, S.G. *et al.* T regulatory cells maintain intestinal homeostasis by suppressing
1279 gammadelta T cells. *Immunity* **33**, 791-803 (2010).

1280
1281 70. Stuart, T. *et al.* Comprehensive Integration of Single-Cell Data. *Cell* **177**, 1888-1902 e1821
1282 (2019).

1283
1284 71. Wolock, S.L., Lopez, R. & Klein, A.M. Scrublet: Computational Identification of Cell
1285 Doublets in Single-Cell Transcriptomic Data. *Cell Syst* **8**, 281-291 e289 (2019).

1286
1287 72. Kowalczyk, M.S. *et al.* Single-cell RNA-seq reveals changes in cell cycle and
1288 differentiation programs upon aging of hematopoietic stem cells. *Genome Res* **25**, 1860-
1289 1872 (2015).

1290
1291 73. Hafemeister, C. & Satija, R. Normalization and variance stabilization of single-cell RNA-
1292 seq data using regularized negative binomial regression. *Genome Biol* **20**, 296 (2019).

1293
1294 74. Zhang, X. *et al.* CellMarker: a manually curated resource of cell markers in human and
1295 mouse. *Nucleic Acids Res* **47**, D721-d728 (2019).

1296
1297 75. Franzén, O., Gan, L.M. & Björkegren, J.L.M. PanglaoDB: a web server for exploration of
1298 mouse and human single-cell RNA sequencing data. *Database (Oxford)* **2019** (2019).

1299

76. Finak, G. *et al.* MAST: a flexible statistical framework for assessing transcriptional changes and characterizing heterogeneity in single-cell RNA sequencing data. *Genome Biol* **16**, 278 (2015).

77. La Manno, G. *et al.* RNA velocity of single cells. *Nature* **560**, 494-498 (2018).

78. Bergen, V., Lange, M., Peidli, S., Wolf, F.A. & Theis, F.J. Generalizing RNA velocity to transient cell states through dynamical modeling. *Nat Biotechnol* **38**, 1408-1414 (2020).

79. Van de Sande, B. *et al.* A scalable SCENIC workflow for single-cell gene regulatory network analysis. *Nat Protoc* **15**, 2247-2276 (2020).

80. Bolger, A.M., Lohse, M. & Usadel, B. Trimmomatic: a flexible trimmer for Illumina sequence data. *Bioinformatics* **30**, 2114-2120 (2014).

81. Kim, D., Langmead, B. & Salzberg, S.L. HISAT: a fast spliced aligner with low memory requirements. *Nat Methods* **12**, 357-360 (2015).

82. Liao, Y., Smyth, G.K. & Shi, W. featureCounts: an efficient general purpose program for assigning sequence reads to genomic features. *Bioinformatics* **30**, 923-930 (2014).

83. Love, M.I., Huber, W. & Anders, S. Moderated estimation of fold change and dispersion for RNA-seq data with DESeq2. *Genome Biol* **15**, 550 (2014).

84. Fernandes, A.D. *et al.* Unifying the analysis of high-throughput sequencing datasets: characterizing RNA-seq, 16S rRNA gene sequencing and selective growth experiments by compositional data analysis. *Microbiome* **2**, 15 (2014).

85. Gloor, G.B., Macklaim, J.M., Pawlowsky-Glahn, V. & Egozcue, J.J. Microbiome Datasets Are Compositional: And This Is Not Optional. *Front Microbiol* **8**, 2224 (2017).

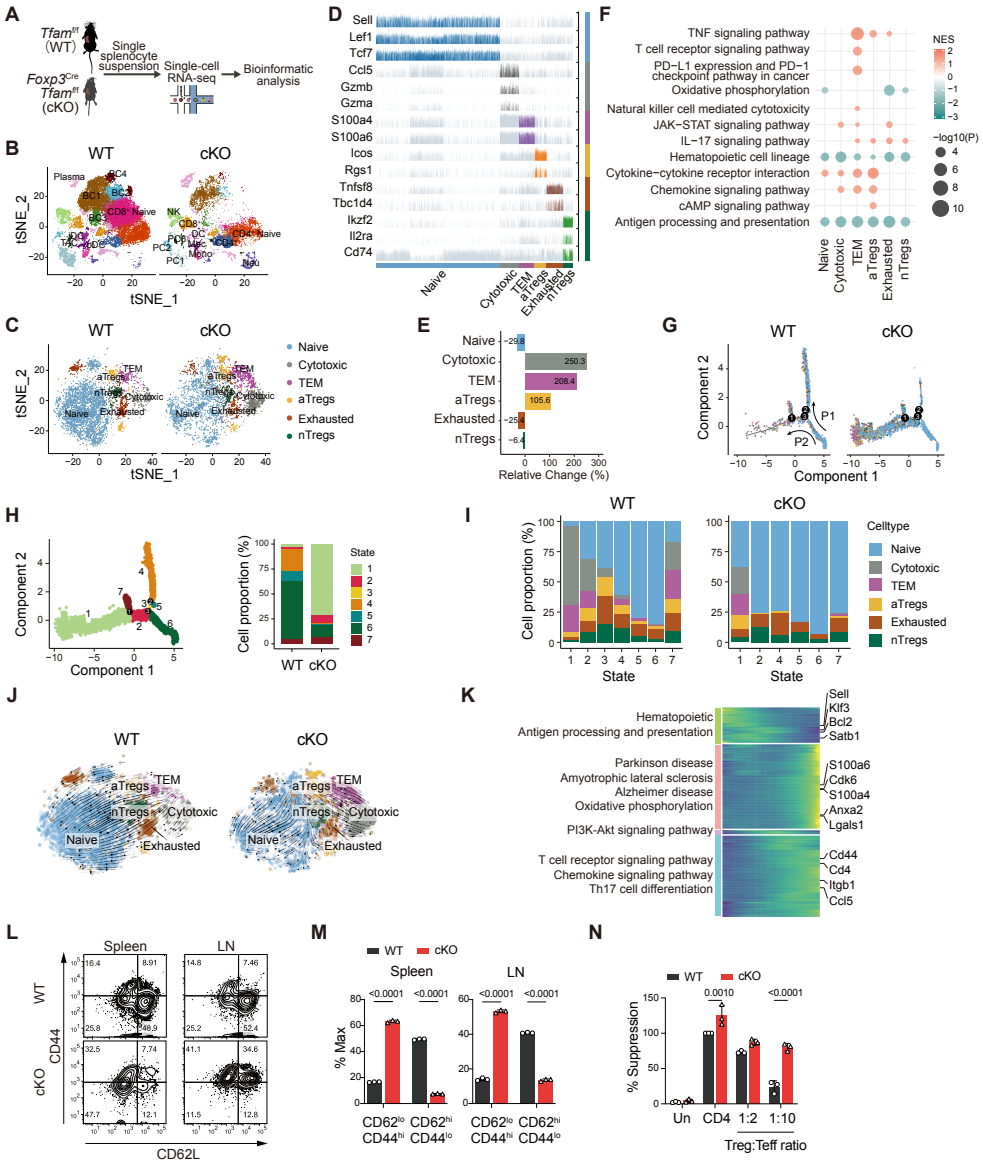

Figure 1. Treg-intrinsic TFAM loss reprograms CD4⁺ T cell lineage fate toward pro-inflammatory and terminal effector states.(**A**) Schematic representation of the experimental workflow. Splenocytes were isolated from Foxp3^{Cre}Tfam$^{f/f}$ (TFAM cKO) and Tfam$^{f/f}$ (WT) mice for single-cell RNA sequencing (scRNA-seq) and downstream analysis. (**B**) UMAP projection of 49,156 immune cells (WT: 34,958; cKO: 14,198), identifying 21 major immune subsets across 26 transcriptional clusters. Erythroid lineage cells were excluded. (**C**) UMAP projection of CD4⁺ T cells (WT: 4,324; cKO: 3,497), revealing six transcriptionally distinct subsets: naïve, effector memory (TEM), exhausted, natural Tregs (nTregs), aged/dysfunctional Tregs (aTregs), and cytotoxic CD4⁺ T cells. (**D**) Track plot showing representative gene expression patterns across single CD4⁺ T cells. Rows represent genes; columns represent individual cells. (**E**) Bar graph quantifying relative abundance of CD4⁺ T cell subsets in WT and cKO mice. TFAM deficiency promotes expansion of effector-like states (aTregs, cytotoxic, and TEM), with reduced naïve and exhausted populations. (**F**) Gene set enrichment analysis (GSEA) of KEGG pathways shows increased TNFα signaling, cytokine/chemokine responses, and calcium flux in CD4⁺ T cells from TFAM cKO mice. (**G**) Pseudotime trajectory analysis (Monocle) of CD4⁺ T cells reveal two dominant differentiation paths (P1 and P2). TFAM-deficient cells preferentially adopt the alternative P2 trajectory, enriched in transcriptional States 1 and 2. (**H**) Monocle 2 trajectory cell states for all CD4+ T cells, each branch represents one cell state (left). Barplots representing cell proportions in the seven states of WT and cKO (right). Cells are colored according to seven states, which partition the trajectory. (**I**) Relative proportion of CD4+ T cells among different states of WT and cKO spleen, color stands for cell type. (**J**) RNA velocity analysis confirms directionality of lineage bifurcation, with streamlines overlaid on UMAP embedding indicating transcriptional flow. (**K**) Heatmap of four gene clusters ordered by pseudotime. Cluster 1 genes (e.g., Klf3, Bcl2) mark early developmental states; Cluster 2 genes (e.g., Ccl5, S100a6) are linked to terminal effector function and inflammation. KEGG pathway enrichment of cluster-specific genes is shown. (**L**) Representative flow cytometry plots of CD4⁺CD44^{hi}CD62L^{lo} effector and CD4⁺CD44^{lo}CD62L^{hi} naïve T cells in spleen and lymph nodes from WT and TFAM cKO mice. (**M**) Quantification of mean fluorescence intensity (MFI) for effector and naïve CD4⁺ T cells across organs. TFAM cKO mice exhibit increased effector T cell signatures. (**N**) Suppression assay showing reduced regulatory function of TFAM-deficient Tregs in vitro. Co-culture with CFSE-labeled CD4⁺ Tconv cells demonstrates impaired suppression of proliferation upon CD3/CD28 stimulation.

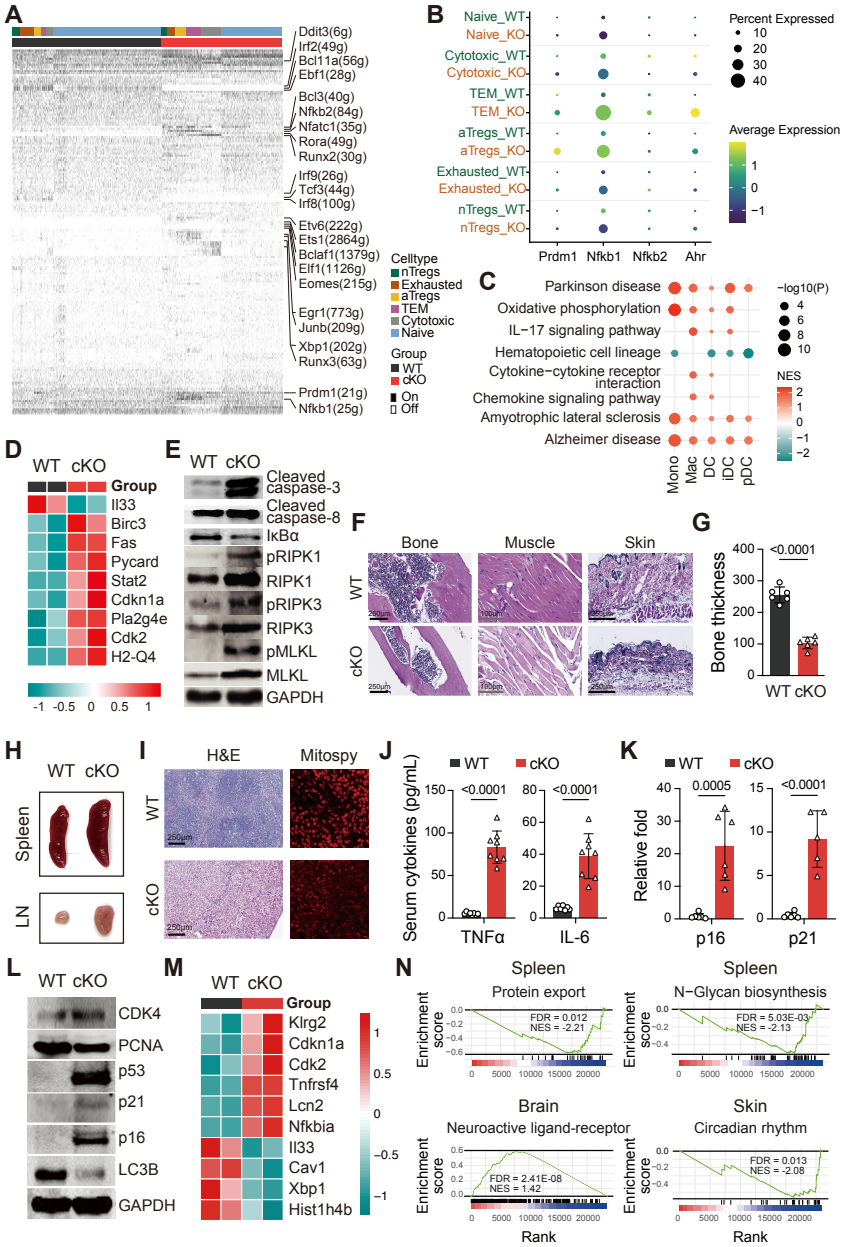

Figure 2. Treg-intrinsic TFAM loss triggers a multi-lineage stress response, inflammatory reprogramming, and systemic senescence. (**A**) Gene regulatory network (GRN) inference from scRNA-seq data identified 177 regulons across CD4⁺ T cell subsets. TFAM cKO Tregs showed increased activity of inflammatory (*Nfkb2*, *Nfatc1*, *Rora*, *Runx2*), stress-responsive (*Egr1*, *Junb*, *Xbp1*), and cytotoxic (*Runx3*) regulons, alongside pan-CD4⁺ expression of the mitochondrial stress gene *Ddit3*. (**B**) Dot plots showing upregulation of key inflammatory transcriptional regulators (*Prdm1*, *Nfkb1*,*Nfkb2*, *Ahr*) in TFAM-deficient Tregs. (**C**) Gene set enrichment analysis (GSEA) shows significant pathways in Monocytes (Mono), Macrophages (Mac), dendritic cell (DC), Immature Dendritic Cells (iDC) and Plasmacytoid Dendritic Cells (pDC) cells in TFAM cKO mice. (**D**) Bulk RNA-seq of cKO spleens revealed enrichment of cell death pathways, including apoptosis and necroptosis. (**E**) Immunoblots confirmed caspase-3 and -8 cleavage, IκBα degradation, and phosphorylation of RIPK1, RIPK3, and MLKL, indicative of RIPK-mediated immunogenic cell death. (**F**) Histological analysis revealed multi-organ inflammatory infiltration in colon, liver, lung, and kidney of TFAM cKO mice. (**G**) H&E staining of femurs showed pronounced cortical bone thinning in TFAM cKO animals. (**H**) Spleens from TFAM cKO mice exhibited splenomegaly, follicular disruption, and marginal zone disorganization. (**I**) Mitospy staining in sorted Tregs revealed mitochondrial depolarization and elevated oxidative stress in TFAM-deficient cells. (**J**) Elevated circulating levels of TNF-α, IL-6, and IFNγ in serum from TFAM cKO mice, confirming systemic inflammation. (**K**) RT-qPCR showed increased expression of Cdkn2a (p16) and Cdkn1a (p21). (**L**) Immunoblotting of splenic lysates confirmed elevated levels of p53, CDK4, PCNA, p16, andp21, consistent with senescence-associated gene expression. (**M**) Whole-spleen RNA-seq revealed enrichment of aging- and inflammation-associated gene networks. (**N**) GSEA showed significant upregulation of pathways linked to neuroactive ligand–receptor signaling, and downregulation of circadian rhythm disruption, and protein trafficking which are hallmarks of systemic immune aging.

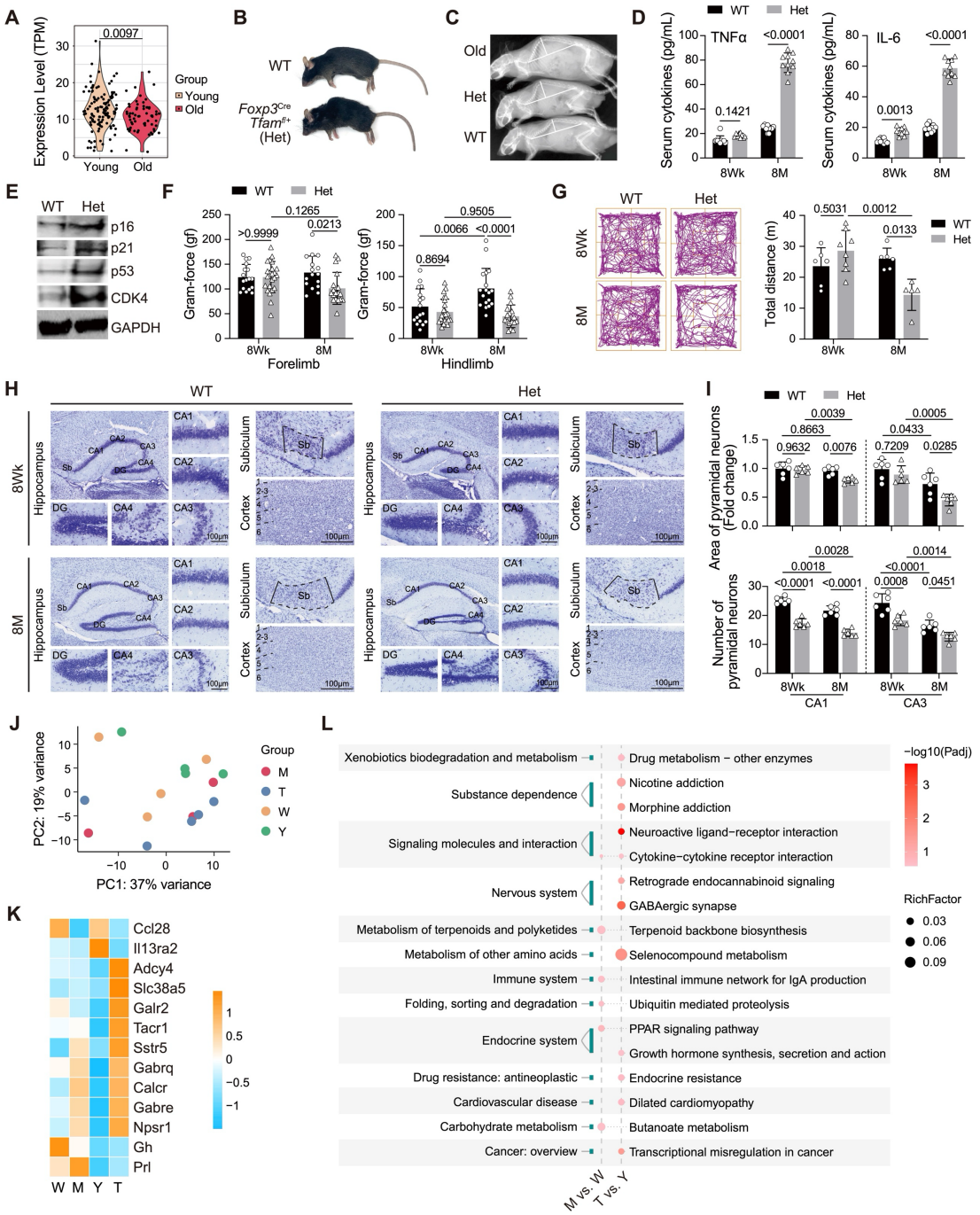

Figure 3. Partial TFAM reduction in Tregs promotes systemic aging features, peripheral inflammation, and early neurodegenerative changes. (**A**) Human PBMC transcriptome analysis reveals age-associated decline in TFAM expression, supporting its role as a mitochondrial-immune rheostat. (**B-C**) TFAM Het (Foxp3CreTfamf/+) mice develop aging phenotypes, including kyphosis and reduced body weight, by 8-10 months of age. (**D**) Circulating TNF-α and IL-6 levels are elevated in TFAM Het mice, indicating persistent low-grade systemic inflammation. (**E**) Splenic CD4$^+$ T cells isolated from TFAM Het mice display elevated expression of senescence-associated markers, including Cdkn2a (*p16^Ink4a*), Cdkn1a (*p21^Cip1*), p53, and CDK4, with GAPDH serving as the loading control. (**F**) Neuromuscular assessment shows reduced forelimb grip strength in TFAM Het mice. (**G**) Open field behavioral assay demonstrates decreased exploratory behavior and locomotor hypoactivity, consistent with CNS dysfunction. (**H–I**) Cresyl violet staining reveals neuronal loss in the hippocampus and cortex of 8-month-old TFAM Het mice compared to 8-week controls. (**J**) Longitudinal hippocampal RNA-seq profiling shows minimal transcriptional changes at 8 weeks but extensive neuroimmune remodeling by 8 months. (**K**) Heatmap displaying upregulation of neuroinflammation-associated genes (*Gabra5*, *Slc38a5*, *Calcr*, *Ganbare*) in 8-month TFAM Het hippocampus. (**L**) KEGG pathway enrichment of 8-month hippocampal transcriptomes identify significant enriched pathways of oxidative stress, inflammatory signaling, and neurodegeneration-linked pathways.

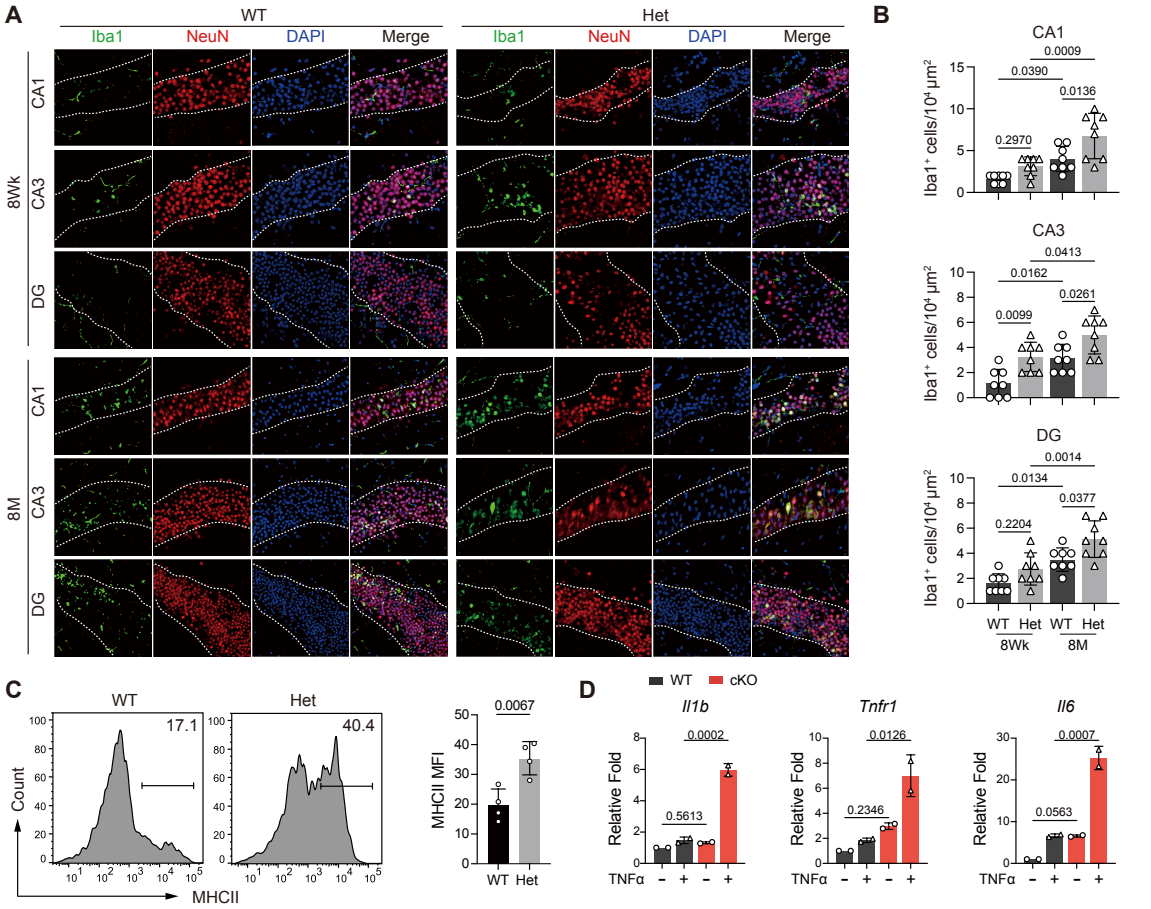

Figure 4. TFAM insufficiency in Tregs triggers CNS immune activation and microglial sensitization to TNF signaling. (**A-B**) Iba1 and NeuN immunohistochemistry shows widespread activation of amoeboid microglia in the cortex and hippocampus of 8-month-old TFAM Het mice, with concurrent neuronal loss.(**C**) Flow cytometric analysis reveals increased MHC-I expression on brain-resident CX3CR1⁺ microglia from TFAM Het mice, consistent with enhanced antigen presentation. (**D**) Ex vivo stimulation with TNF-α induces elevated *Il1b*, *Tnfr1*, and *Il6* expression in CX3CR1⁺ microglia from TFAM Het brains, indicating heightened inflammatory sensitivity.

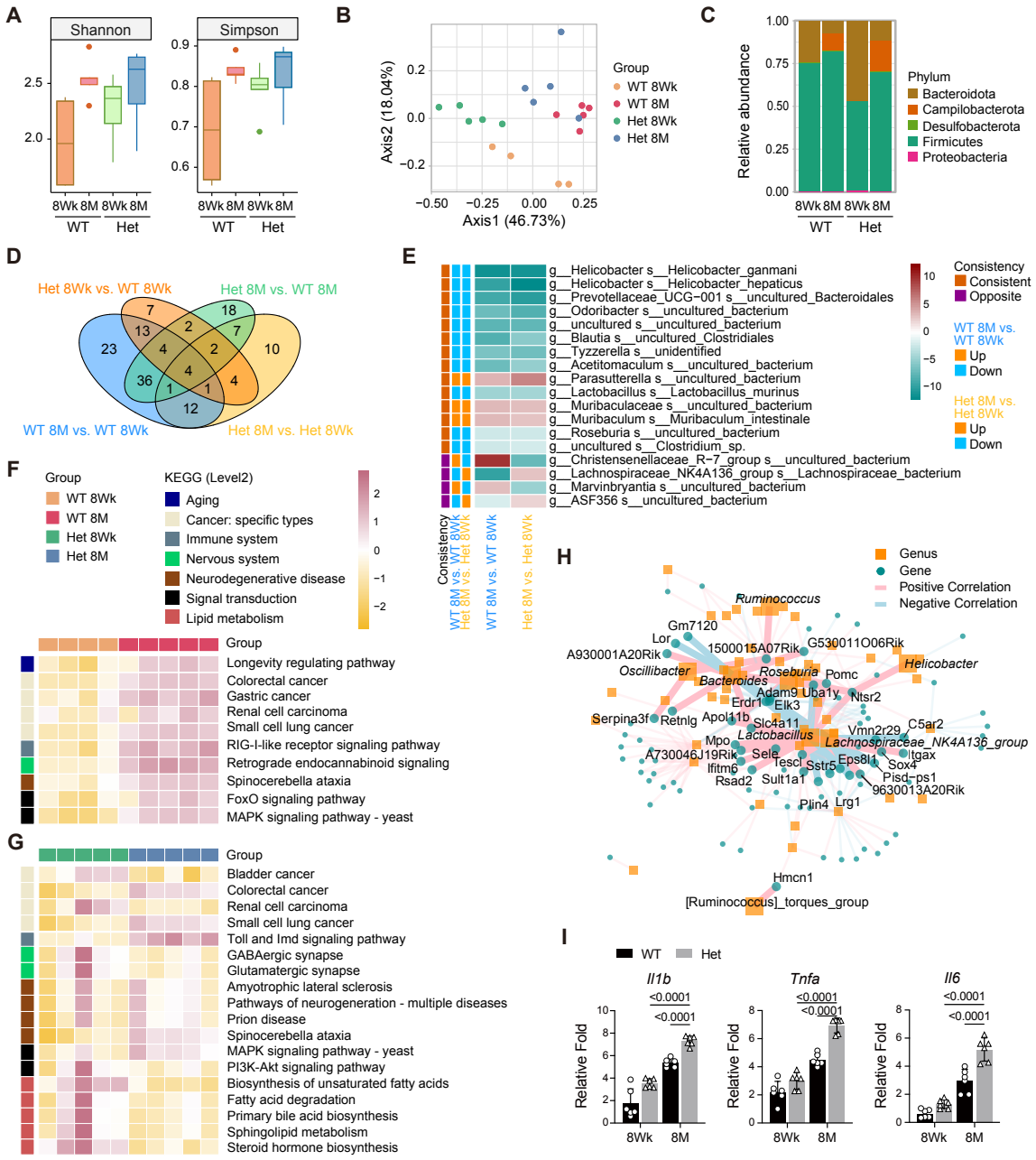

Figure 5. TFAM insufficiency in Tregs drives microbiota–lipid dysregulation and neuroinflammatory reprogramming via the gut–brain–immune axis. (**A**) Longitudinal 16S rRNA sequencing reveals significantly elevated α-diversity (Shannon and Simpson indices) in TFAM Het mice, peaking at 8 months of age. (**B**) β-diversity analysis (Bray–Curtis dissimilarity) demonstrates genotype- and age-specific microbial clustering, indicating progressive community remodeling. (**C**) Phylum-level taxonomic profiling reveals expansion of *Campilobacterota* and depletion of *Bacteroidota* in aged TFAM Het mice, signatures linked to inflammaging. (**D**) VennDiagram depicting distribution and overlap of microbial species across genotypes and age groups. (**E**) Differential abundance analysis identifies 18 significantly altered taxa, including loss of key SCFA-producing genera (*Lactobacillus murinus*, *Odoribacter*, *Prevotellaceae_UCG-001*) in TFAM Het mice. (**F**) KEGG-based predictive metagenomics shows TFAM Het microbiota enriched in age-related pathways including FoxO, and spinocerebellar ataxia signaling. (**G**) Lipid metabolism pathways, including unsaturated fatty acid biosynthesis, bile acid biosynthesis, and sphingolipid metabolism, are significantly altered. Neurotransmission pathways (GABAergic, glutamatergic synapses) are also enriched in aged TFAM Het mice. (**H**) Microbiota–host gene co-correlation network analysis reveals 323 significant interactions. Notably, *Helicobacter* positively correlates with *Ntsr2*, while Lactobacillus inversely correlates with neuroendocrine (e.g., *Pomc*, *Sstr5*) and developmental genes (*Elk3*, *Sox4*) and positively correlates with inflammatory genes (*Mpo*, *Ifitm6*). *Lachnospiraceae_NK4A136_group* links to complement-mediated inflammation (*C5ar2*). (**I**) RT-qPCR validation confirms elevated expression of *Il1b* and *Tnfr1* in peripheral tissues from TFAM Het mice, supporting a chronic inflammatory state.

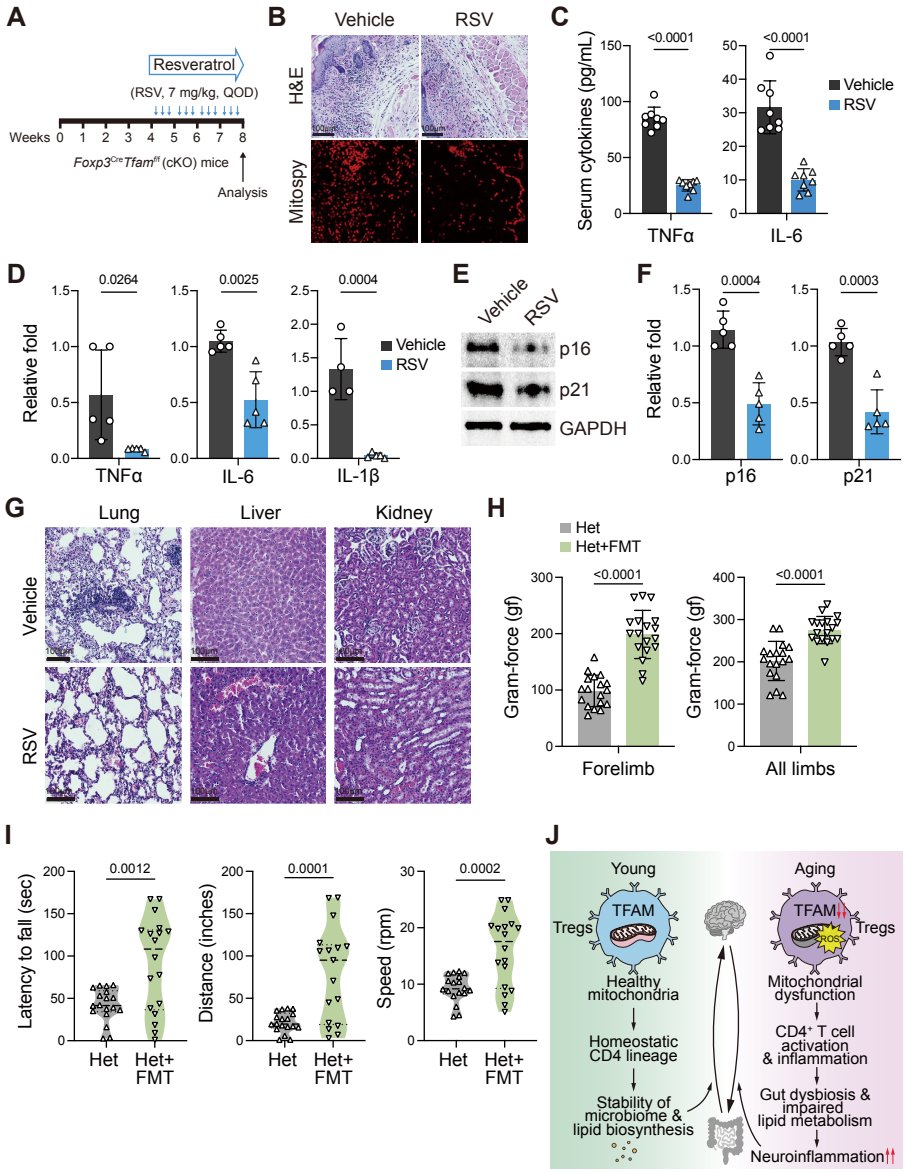

Figure 6. Restoration of mitochondrial fitness mitigates inflammation and functional decline in models of immune aging. (**A**) Schematic of therapeutic intervention in TFAM cKO mice. Mice received intraperitoneal resveratrol (RSV; 7 mg/kg) every other day for 4 weeks. (**B**) Mitospy staining in skin tissue reveals enhanced mitochondrial membrane potential in RSV-treated TFAM cKO mice, indicating improved mitochondrial integrity. (**C**) Serum levels of TNF-α and IL-6 were significantly reduced following RSV treatment, reflecting dampened systemic inflammation. (**D-F**) Quantitative RT-PCR analysis of splenocytes shows reduced expression of senescence markers Cdkn2a (p16Ink4a) and Cdkn1a (p21Cip1) in RSV-treated mice, consistent with suppression of the senescence-associated secretory phenotype (SASP). (**G**) Histological examination of lung, liver, and kidney shows decreased inflammatory infiltration and preserved tissue structure in RSV-treated animals. (**H**) Experimental design for fecal microbiota transplantation (FMT) in TFAM Het mice. Mice were antibiotic-conditioned for 10 days and subsequently gavage with feces from TFAM-sufficient donors over 3 days, followed by a 3-week recovery. (**I**) FMT improved neuromuscular performance, demonstrated by increased rotarod endurance and forelimb grip strength. These improvements were associated with re-expression of Treg-associated genes and suppression of pro-inflammatory programs. (**J**) Working model summarizing the role of TFAM as a central regulator of mitochondrial redox balance, microbiota composition, and immune aging. Restoration of mitochondrial integrity via RSV and microbial reprogramming via FMT ameliorates immunopathology and rejuvenates immune function.

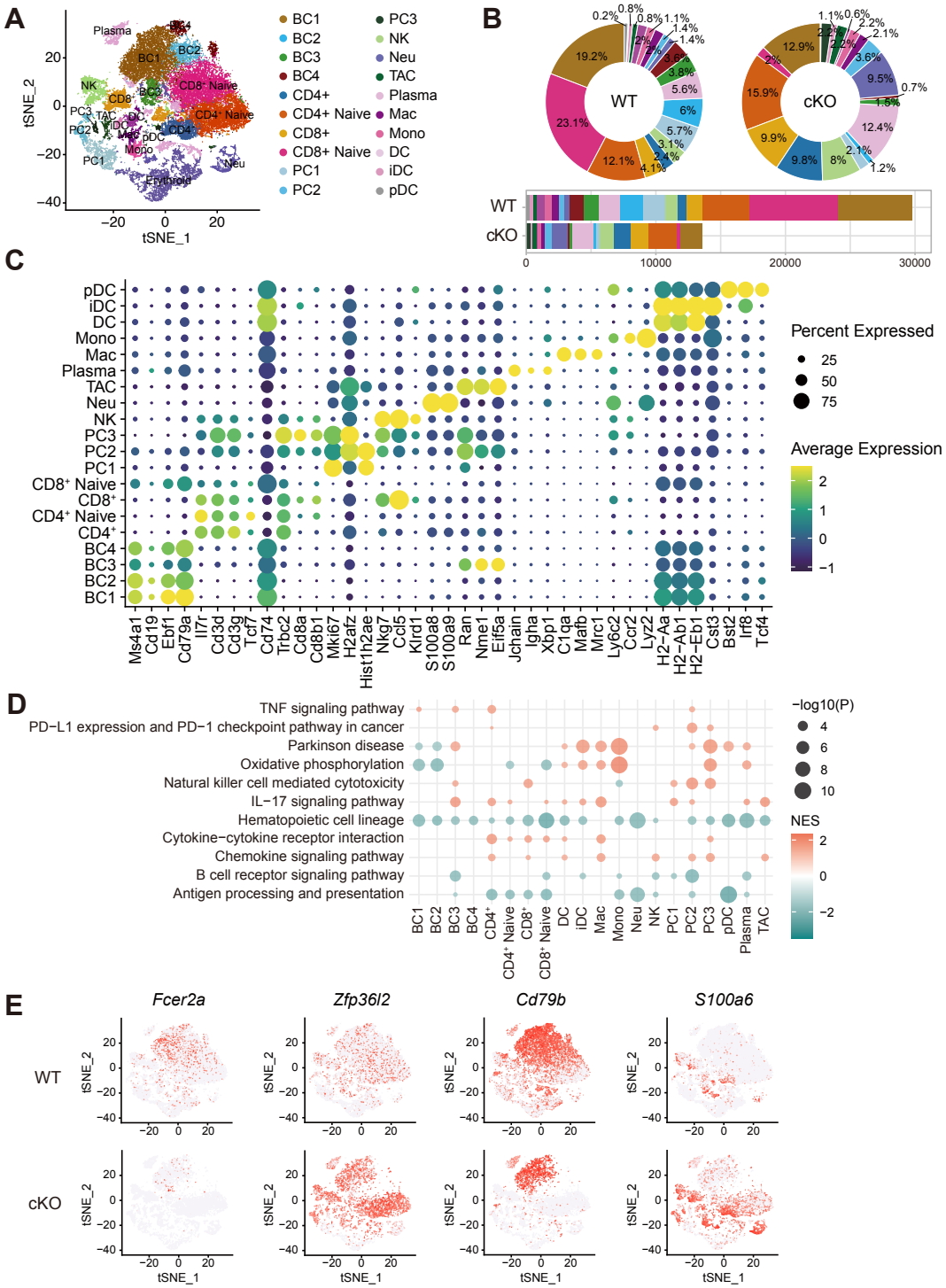

Supplementary Fig. 1: Landscape of scRNA-seq analysis of WT and cKO spleen. A. t-SNE projections of single-cell transcriptomes from WT and cKO mice before Erythroid cells were removed, annotated by cell type. Each dot denotes a distinct cell. **B.** Cell subset proportions (top) and numbers (bottom) for WT and cKO spleens. **C.** Dot plot of mean expression of canonical marker genes for 20 major lineages from tissues of each origin, as indicated. **D.** Gene Set Enrichment Analysis (GSEA) of KEGG pathways for all cell types between cKO and WT (Only age-related pathways are selected). Color stands for the up-regulated (red) or down-regulated (blue) in cKO spleen. Enriched terms were identified as significant at a p-value ≤ 0.01. **E.** Expression of aged-related genes (*Fcer2a*, *Cd79b*, *Zfp36l2*, and *S100a6*) on Figure 1B t-SNE embedding. Each dot corresponds to a single cell.

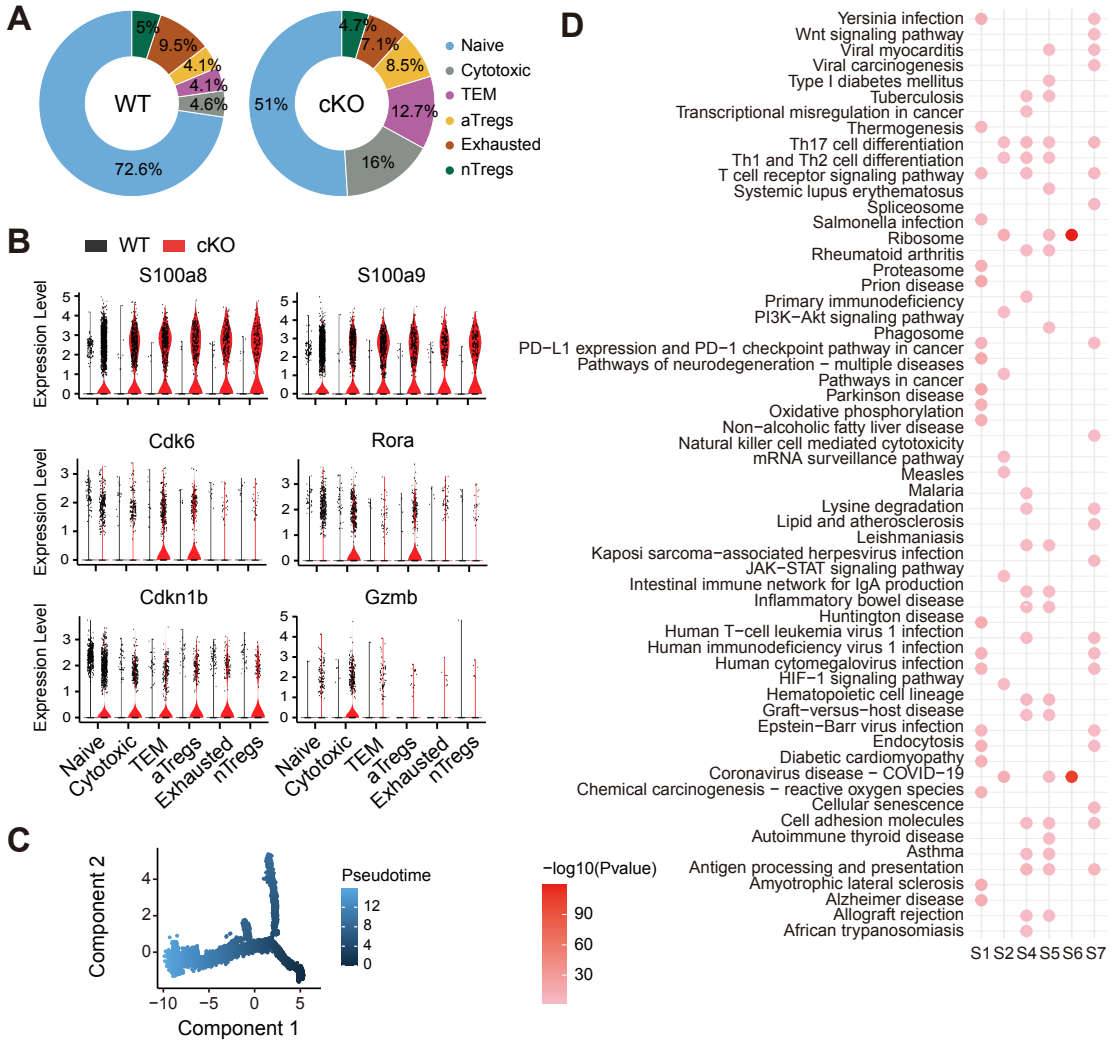

Supplementary Fig. 2: scRNA-seq results show the cellular heterogeneity in CD4⁺ T cells.
A. Relative proportion of CD4⁺ T cells among WT and cKO spleen, color stands for cell type. **B.** Violin plot showing the expression profile of age-related genes among all CD4⁺ T cells. **C.** Monocle 2 prediction of CD4⁺ T cell subsets developmental trajectory with pseudotime. Each dot represents an individual cell. **D.** Functional enrichment analysis of KEGG pathways with up-regulated differential expressed genes for the cell states. Only the top 20 of the enriched pathways were plotted from each state.

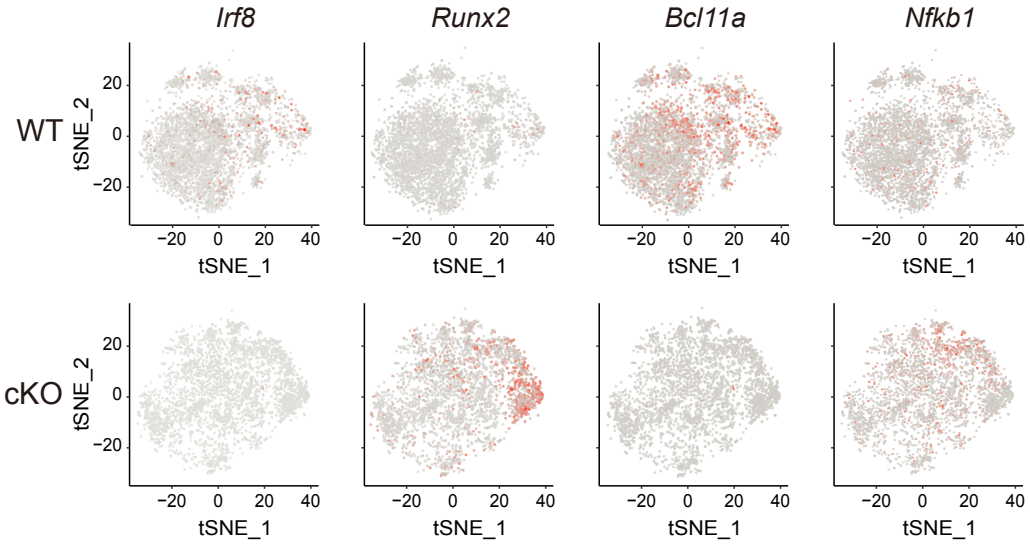

Supplementary Fig. 3: t-SNE projection of binary regulon activity. t-SNE plots visualize the binarized regulon activity states of Irf8, Runx2, Bcl11a, and Nfkb1 across single cells, highlighting distinct transcriptional regulatory modules and cell-type-specific activation patterns.

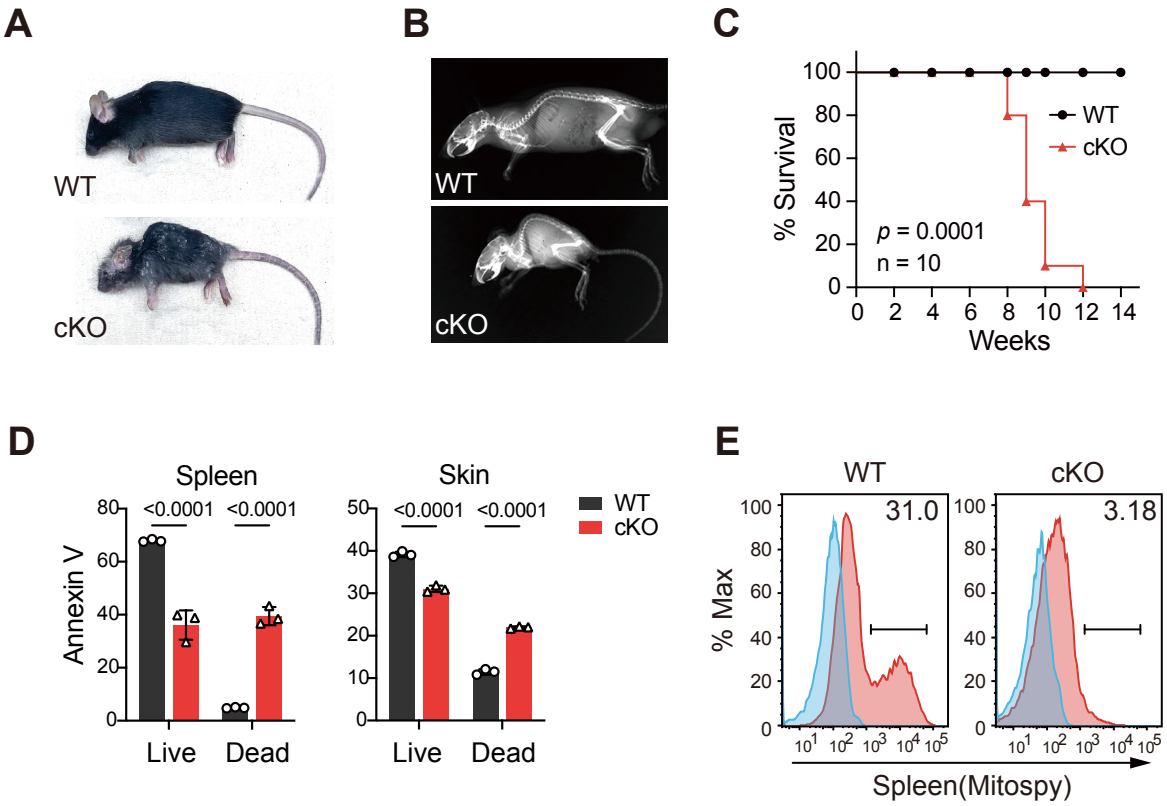

Supplementary Fig. 4: TFAM deletion in Foxp3⁺ Tregs induces systemic pathology and accelerates immune aging in Foxp3^{Cre}Tfam$^{f/f}$ mice. A. Representative photograph showing the deteriorated physical appearance of a cKO mouse (right) compared to an age- and sex-matched WT littermate (left) at 8 weeks of age. **B.** X-ray image depicting increased spinal curvature in the cKO mouse (right) relative to a WT littermate (left) of the same age and sex. **C.** Kaplan-Meier survival analysis comparing WT (n=10; M/F) and cKO (n=10; M/F) mice, revealing reduced lifespan in cKO animals. **D.** Flow cytometric analysis of Annexin V staining in spleen and skin cells from WT and cKO mice, indicating increased cell death in cKO tissues. **E**. Mitospy staining of splenocytes from WT and cKO mice, assessed by flow cytometry and presented as a fluorescence intensity histogram, showing mitochondrial alterations in cKO cells.

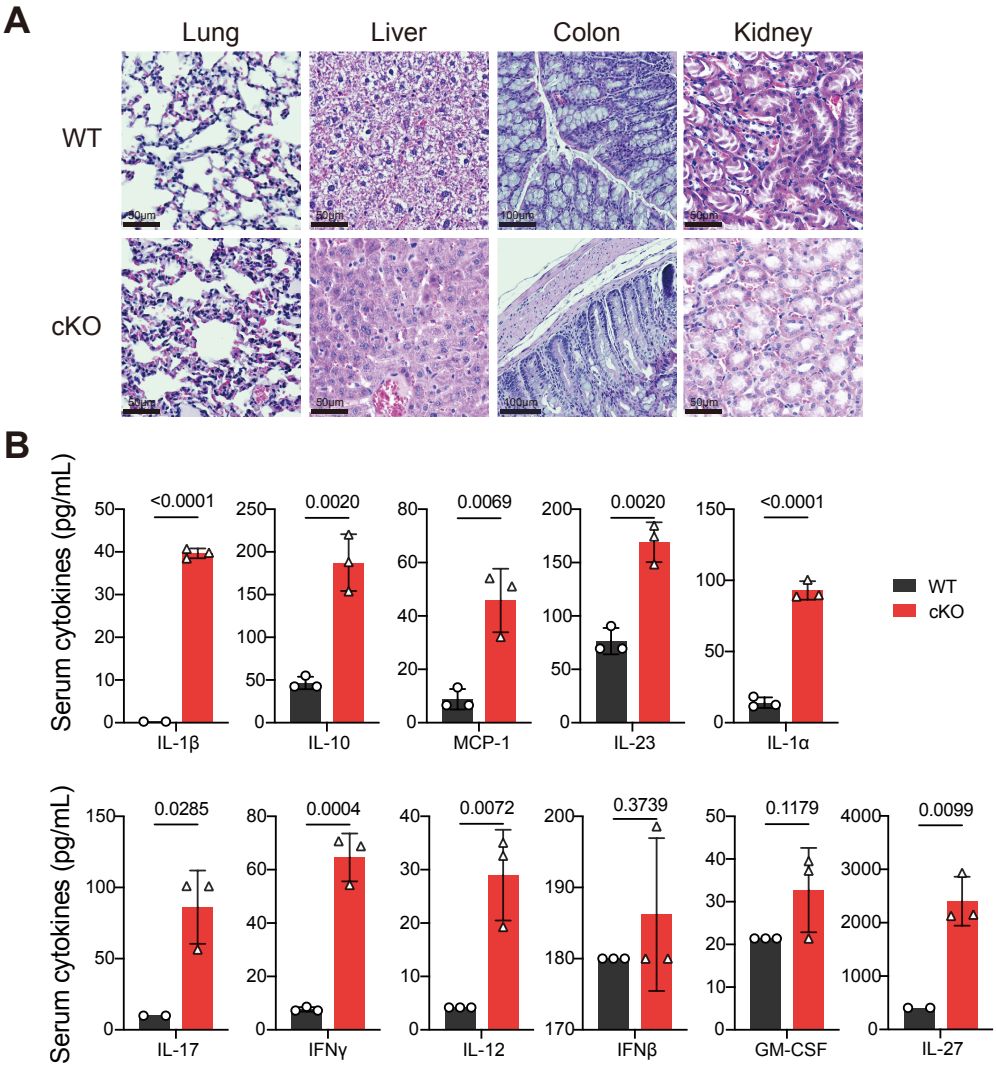

Supplementary Fig. 5: Increased cell infiltration and inflammation in different organs in Foxp3^{Cre}Tfam$^{f/f}$ mice. A. Histology sections stained with H&E from lung, liver, colon, and kidney. **B.** Serum cytokines identified by Legend plex for IL-1β, IL-10, MCP1, IL-23, IL-1α, IL-17, IFNγ, IL-12, IFNβ, GM-CSF, and IL-27 with estimated values displayed. Data represented as mean ± SD. Statistical test used: t-test, WT (n=5-10; M/F) and cKO mice (n=5-10, M/F).

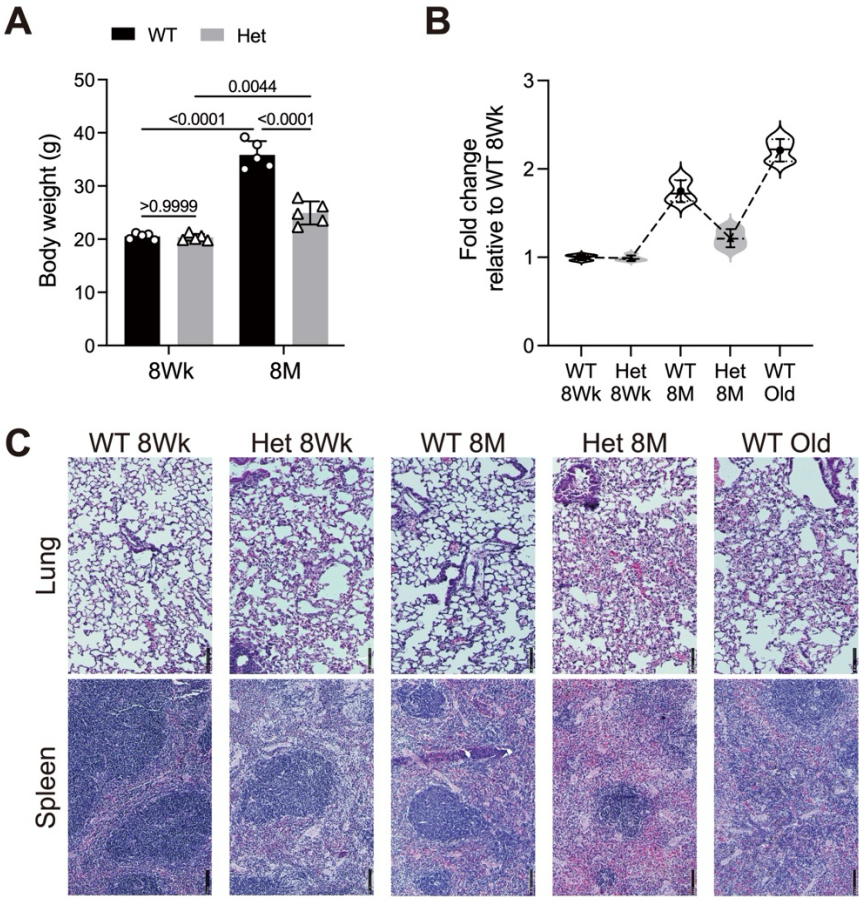

Supplementary Fig. 6: Restoration of mitochondrial function leads to mitigate pathologies.
A-B. Body weight (**A**) and fold change (**B**) of young and old WT and cKO mice. Data represented as mean ± SD. Statistical test used: two-way ANOVA with post-hoc test (**B**). WT (n=5; M/F) and Het mice (n=5, M/F). (**C**) Representative images of H&E histology in spleen and lung from WT (8 weeks, 8 months, and 3 years) and Het (8 weeks and 8 months) mice.